On the influence of grain shape on the cumulative deformations in sand under drained high-cyclic loading

T. Wichtmann,[i)] Th. Triantafyllidis,[ii)] L. Späth[iii)]

Abstract: The cumulative response of three granular materials with significantly different grain shape and surface characteristics (glass beads, natural sand with subrounded grains and crushed sand with very angular particles) but identical grain size distribution curve has been studied in drained cyclic triaxial tests. For each material several tests with 100,000 cycles and different amplitudes, densities, average mean pressures and average stress ratios have been performed. In case of glass beads and natural sand, an approximately square relationship between the residual strain accumulation rates and stress or strain amplitude was found ($\dot{\varepsilon}^{\mathrm{acc}} \sim (\varepsilon^{\mathrm{ampl}})^2$), while an almost proportional dependence was measured for the crushed sand ($\dot{\varepsilon}^{\mathrm{acc}} \sim \varepsilon^{\mathrm{ampl}}$). The largest differences in the cumulative response of the three tested materials were observed regarding the pressure-dependence of $\dot{\varepsilon}^{\mathrm{acc}}$. For glass beads and (less pronounced) for natural sand, the residual strain accumulation rates decrease with average mean pressure, while the opposite tendency was obtained for the crushed sand. At small pressures, the residual strains were much larger for the glass beads than for the natural sand and particularly the crushed sand, while these differences in the accumulated strains almost diminished at larger pressures. Independent of the shape and the surface characteristics of the particles, the average stress ratio could be confirmed as the governing parameter of the 'cyclic flow rule'. Finally, the parameters of the high-cycle accumulation (HCA) model proposed by Niemunis et al. (2005) are analyzed in dependence of grain shape parameters (aspect ratio, circularity) obtained from an automated grain shape analysis.

Keywords: high-cyclic loading; grain shape; glass beads; natural sand; crushed sand; drained cyclic triaxial tests

1 Introduction

A high-cyclic loading, i.e. a loading with a large number of cycles ($N > 10^3$) and relative small strain amplitudes ($\varepsilon^{\mathrm{ampl}} < 10^{-3}$) may be caused by traffic (high-speed trains, magnetic levitation trains), industrial sources (crane rails, machine foundations), wind and waves (on-shore and off-shore wind power plants, coastal structures), repeated filling and emptying processes (locks, tanks and silos), construction processes (e.g. vibration of sheet piles) or mechanical compaction (e.g. vibratory compaction). Permanent deformations caused by such high-cyclic loading may endanger the serviceability of foundations and thus must be accurately predicted in the design stage.

The high-cycle accumulation (HCA) model of Niemunis et al. [51] may be used for that purpose. It is based on numerous drained cyclic tests performed on quartz sands with subrounded particles [82,84–87]. The equations of the HCA model are summarized in the Appendix. Applications of the HCA model, amongst others to offshore wind power plant foundations, are documented e.g. in [18,53,83,91,104–107]. For a simplified calibration of the parameters of the HCA model correlations with the grain size distribution curve (mean grain size d_{50}, uniformity coefficient C_u) or index properties from simple laboratory tests (minimum void ratio $e_{\min}$) have been proposed [88,93,94]. However, an estimation of all parameters from the correlations is recom-

mended for rough estimations only since the equations are valid only for the subrounded quartz sand used in the corresponding experimental study, i.e. they do not consider the influences of grain shape or surface characteristics so far. A combined procedure, where some of the parameters are estimated from the correlations and some others are determined from a single cyclic triaxial test is proposed as the minimum standard for the HCA model calibration [94].

The experimental study documented in this paper represents a first step in order to extend the simplified procedure for the HCA model calibration by the influence of grain shape. Since almost no respective test data can be found in the literature so far, the present study was dedicated to a fundamental examination of the influence of grain shape on the cumulative response under drained high-cyclic loading. Three materials with significantly different grain shape and surface roughness, i.e. glass beads, a natural sand with subrounded grains and a crushed sand with very angular particles have been chosen for this investigation. The strong influence of the grain size distribution curve [88,93,94] was eliminated by producing special mixtures of all three test materials having the same grain size distribution curve. Beside the drained cyclic tests some reference tests with monotonic loading have been also performed.

The characteristics of the particles, i.e. shape, surface profile and roughness, can be examined at different scales, see Figure 1. It is hard to define clear boundaries between these scales, since the transition is smooth. The parameters applied for a quantitative description of the particle shape in this study (an explanation is given in Section 2) are affected by both, the general shape and the surface profile of the particles (schemes on the left-hand side and in the middle of Figure 1). A quantitative description of the sur-

---
[i)] Professor, Chair for Geotechnical Engineering, Bauhaus University Weimar, Germany (corresponding author). Email: torsten.wichtmann@kit.edu
[ii)] Professor and Director of the Institute of Soil Mechanics and Rock Mechanics (IBF), Karlsruhe Institute of Technology (KIT), Germany
[iii)] Master student, Institute of Soil Mechanics and Rock Mechanics, Karlsruhe Institute of Technology, Germany

face roughness (right-hand side of Figure 1) is a matter of ongoing research at the IBF and not a topic of the current paper. However, the shape of the sand particles and its surface roughness are often related to each other, i.e. angular particles usually have a rough surface while rounded grains possess a smooth one [29].
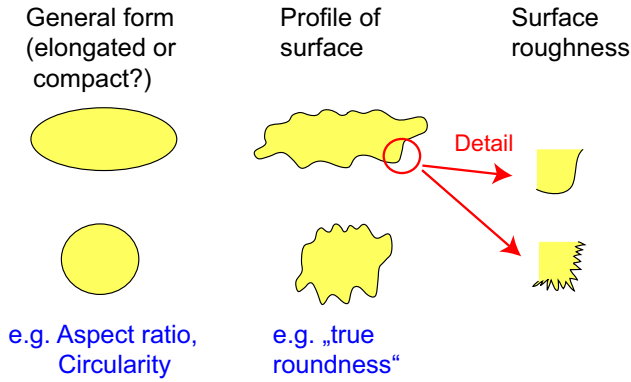
Fig. 1: *Different scales of particle shape or surface roughness (adapted from Santamarina [64])*

2 Tested materials

The particles of all three materials are composed of quartz. The natural sand is a fluvially deposited quartz sand obtained from a sand pit near Dorsten, Germany. The crushed quartz sand originates from crushing of Rhine gravel. It was obtained from a gravel pit near Karlsruhe, Germany. The glass beads used in this study are commercially distributed by the company "Worf Glaskugeln" in Mainz, Germany.

Pictures of the grains of the three different materials taken with an electron scanning microscope are provided in Figure 2. In this test series, the characteristics of the particles on all three scales shown in Figure 1 have been varied simultaneously. From the crushed sand over the natural sand to the glass beads, the shape becomes more compact and more circular, the surface gets less profiled and the surface roughness decreases.

First, each of the three different raw materials glass beads, natural sand and crushed sand was decomposed into several grain sizes by sieving. Next, mixtures with the grain size distribution curve shown in Figure 3 ($d_{50} = 0.6$ mm, $C_u = 1.5$) have been produced for each material. The minimum and maximum void ratios derived from standard tests according to German standard code DIN 18126 (loose placement with a funnel for $e_{\max}$, layerwise compaction under water for $e_{\min}$) as well as the grain densities ϱ_s are summarized in Table 1. Larger void ratios $e_{\max}$ and $e_{\min}$ for granular materials with more angular grains as evident from Table 1 have been also reported in [9, 32, 59, 68, 70, 74, 80]. They are a result of the asperities of the more angular particles which prevent a denser packing. The increase of the range $e_{\max} - e_{\min}$ with increasing angularity is in accordance with [9, 47, 59].

In order to derive quantitative measures for the grain shape, an analysis using the software ImageJ in combination with the Plugin Particles 8 has been performed, in analogy to the procedure described by Cox & Budhu [12] (applied also in [23, 40]). Such automated analysis gives objective values, in contrast to a manual grain shape analysis using graphical charts (e.g. [9, 35, 36, 55, 58]).

For each fraction involved in the grain size distribution curve shown in Figure 3 (e.g. 0.1-0.125 mm, 0.125-0.16 mm, etc.), images of several hundreds of grains were taken with a flat bed scanner (resolution 9600 dpi). These images were converted to a black-and-white format before being analyzed. All particles on the figure having a size in accordance with the grain fraction under consideration (no dust particles or similar should be analyzed) and lying separately (i.e. without any contact to neighboured grains, in order to prevent the analysis of conglomerates of several grains) were identified by the software. The cross-sectional area, perimeter, geometric centre of gravity, etc. of the individual grains measured in pixels were determined. Based on this information, several geometric parameters describing the shape of the particles could be calculated. Two shape parameters are used further in this paper: Aspect Ratio and Circularity. Aspect Ratio is defined as the ratio of the length F of the longest axis divided by the length B of the largest dimension in the orthogonal direction (see schemes in Figure 4). Circularity is obtained as the ratio of the cross-sectional area of the grain A_{Grain} divided by the area A_{Circle} of a circle having the same perimeter as the original grain (Figure 4). Circularity is thus a measure of how much the shape of a grain resembles a circle. It should be kept in mind, however, that this analysis is restricted to two-dimensional images of the grains, not evaluating their third dimension.

For each fraction of a certain material, several hundreds of grains have been analyzed in this way. Mean values of the shape parameters of all grains within a fraction have been considered further. These mean values have been weighted by the mass fraction of that grain size in order to obtain a single value of the shape parameter for each material. These mean values of Aspect Ratio and Circularity are summarized in Table 1. Evidently, Circularity increases from the crushed sand over the natural sand to the glass beads, while Aspect Ratio simultaneously decreases.

3 Monotonic tests

Several drained monotonic triaxial tests with different initial densities $I_{D0} = (e_{\max} - e_0)/(e_{\max} - e_{\min})$, with e_0 being the void ratio prior to shearing, and an isotropic initial stress with an effective mean pressure $p_0 = 100$ kPa ($p = (\sigma_1' + 2\sigma_3')/3$) have been performed on each test material. A standard triaxial cell for monotonic testing (not shown herein) has been used. The samples measuring 10 cm in diameter and 10 cm in height (see a discussion of the influence of sample geometry in Section 6) were prepared by dry air pluviation using a funnel. Different densities were achieved by choosing different outlet diameters of the funnel. The fall height between the outlet and the actual sample surface has been kept constant (about 2 cm) during pluviation. After preparation the samples were saturated with de-aired water. A back pressure of 500 kPa was applied in all tests. The quality of saturation was checked by Skempton's B-value. B-values larger than 0.99 were achieved in all tests.

The diagrams in Figure 5a,b provide curves of deviatoric stress $q = \sigma_1 - \sigma_3$ or volumetric strain $\varepsilon_v = \varepsilon_1 + 2\varepsilon_3$ versus axial strain ε_1 for loose and dense samples. The fluttering $q(\varepsilon_1)$ curves of the glass beads are in good accordance with [75, 108]. They are a result of the stick-slip response of a packing of round particles that favour rolling, thus forming an unstable microstructure [81]. Beside a larger initial
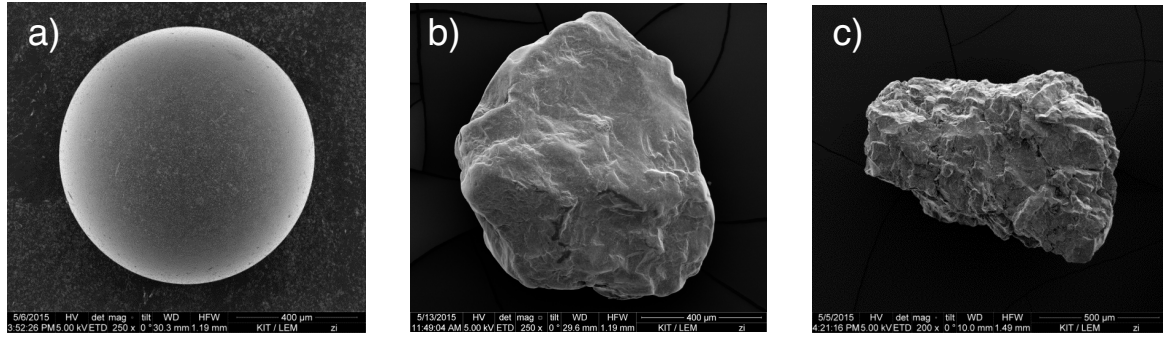
Fig. 2: *Pictures of grains of a) glass beads, b) natural sand and c) crushed sand taken with an electron scanning microscope [17]*

Material	d_{50} [mm]	C_u [-]	ϱ_s [g/cm^3]	$e_{\min}$ [-]	$e_{\max}$ [-]	Aspect Ratio	Circularity
Glass beads	0.60	1.5	2.52	0.530	0.700	1.07	0.89
Natural sand	0.60	1.5	2.65	0.571	0.891	1.23	0.79
Crushed sand	0.60	1.5	2.66	0.763	1.149	1.31	0.73

Table 1: Mean grain size d_{50}, uniformity coefficient $C_u = d_{60}/d_{10}$, grain density ϱ_s, minimum and maximum void ratios $e_{\min}$, $e_{\max}$ and grain shape parameters Aspect Ratio and Circularity for the three tested materials
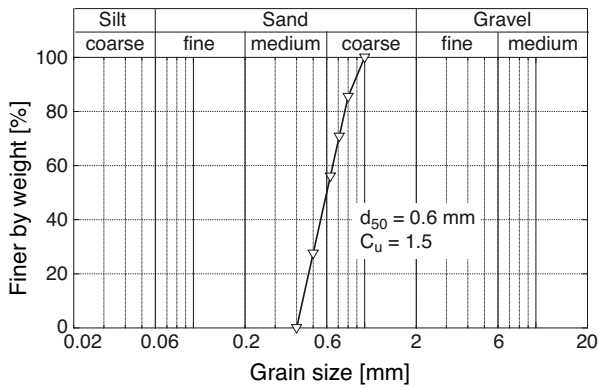
Fig. 3: *Tested grain size distribution curve (identical for all three test materials)*
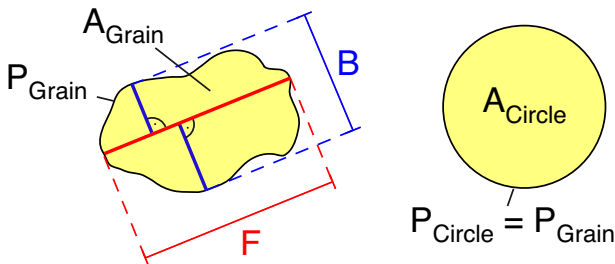
Fig. 4: *Definition of grain shape parameters Aspect Ratio = F/B and Circularity = A_{Grain}/A_{Circle}*

stiffness of the glass beads, an increase of shear strength with increasing angularity of the granular material is evident in Figure 5a. Regarding the volumetric response, both the initial contraction and the subsequent dilatancy are larger for the more angular materials (Figure 5b). In case of the glass beads, the contractive phase at the beginning of shearing is extremely small.

The increase of the shear strength with increasing particle angularity is also confirmed by the diagram in Figure 5c, giving the peak friction angle φ_P as a function of initial relative density. It agrees well with the literature [3, 7, 9, 20, 22, 29, 32, 40, 47, 48, 52, 59, 60, 67, 68, 70, 74, 75, 99, 108]. A higher angularity and surface roughness of the grains leads to a higher interparticle friction and interlocking between the particles, providing restraint to particle sliding and rotation during deformation. The increased interparticle friction and the restricted particle mobility allows the application of higher shear stresses to assemblies of more angular particles [9, 22, 43, 48, 74].

As a measure of the initial stiffness, Young's modulus E_{50} is presented as a function of I_{D0} in Figure 5d. E_{50} represents a secant stiffness between $q = 0$ and $q = q_{\max}/2$. The data in Figure 5d corroborates the reduction of the initial stiffness with increasing particle angularity. Similar tendencies are also reported in [9, 48, 70], partially based on oedometric tests. The lower stiffness for materials with more angular particles can be explained by the fact that those materials possess a higher void ratio at same relative density, due to the larger $e_{\max}$ and $e_{\min}$ values addressed above. The looser packing and the accompanying lower coordination number results in a softer matrix and thus a higher compressibility [9, 48].

While shearing more angular granular materials, larger values of shear stress and strain are necessary to break interlocking and allow dilatancy. This is reflected by the later onset of dilatancy in the tests on the crushed sand (Figure 5b). The lower dilatancy angles of the crushed sand (Figure 5e) correspond to the smaller maximum inclination of the $\varepsilon_v(\varepsilon_1)$ curves (Figure 5b), cf. [40,79,108], although the overall dilatancy (final value of volumetric strain ε_v, see Figure 5b) gets more pronounced with increasing angularity. The higher shear strength for the materials with more angular particles goes along with a higher stress ratio η_{c-d} at the onset of dilatancy (Figure 5f, with $\eta = q/p$). In contrast to [22], η_{c-d} has been found almost unaffected by density for all three tested grain shapes.

3
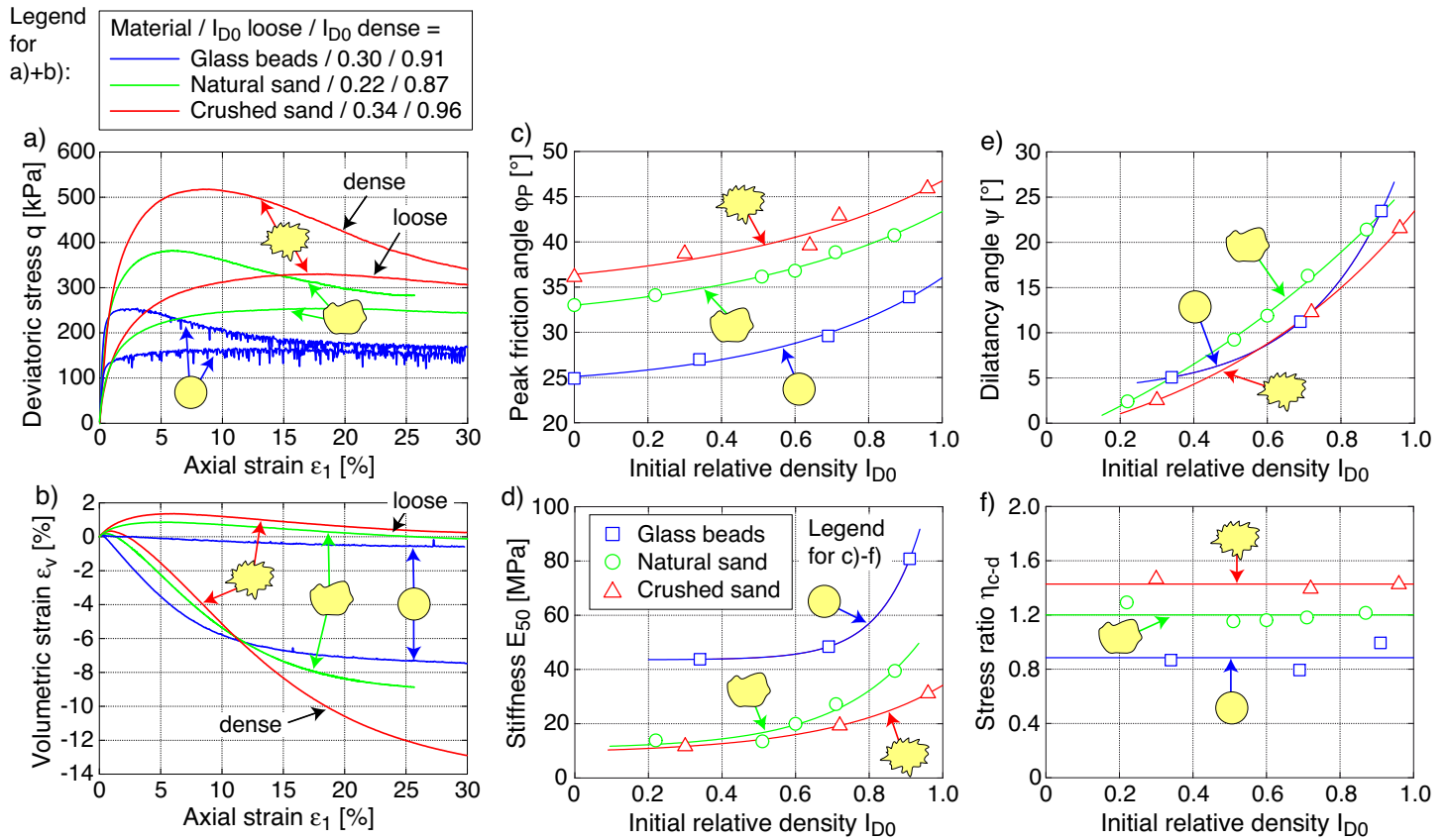
Fig. 5: a) Stress-strain curves $q(\varepsilon_1)$, b) volumetric strain $\varepsilon_v(\varepsilon_1)$, c) density-dependent peak friction angle φ_P, d) Young's modulus E_{50}, e) dilatancy angle ψ and f) stress ratio η_{c-d} at the onset of dilatancy obtained from drained monotonic tests on the three test materials with different grain shape

As further addressed in Section 5 particle breakage effects can be regarded as negligible in the present test series.

4   Cyclic tests
4.1   Test device, testing procedure and analysis of results

A scheme of the cyclic triaxial device used for this study is given in Figure 6. This device has been designed and manufactured with the aim to enable tests with very large numbers of cycles. The sample is encompassed in a pressure cell being capable for pressures up to 1000 kPa. A pneumatic loading system is used to apply the axial loading. The pneumatic cylinder is located at the bottom of the test device, so that the axial loading is applied in the upwards direction. This arrangement enables a sample preparation inside the test device, i.e. the sample is prepared directly on the load piston (see the photos in Figure 7). The top end plate of the sample is rigidly connected with the upper plate of the loading frame, which is decoupled from the lid of the pressure cell. The bottom and the top end plate are both equipped with a central porous stone of 15 mm diameter. The drainage lines from these porous stones are connected to a burette used for the measurement of volume changes. As in the monotonic tests, samples with a diameter of 100 mm and a height of 100 mm were used in the present test series. The influence of the sample geometry in the cyclic tests is further discussed in Section 6. In order to eliminate end friction effects, smeared end plates composed of a layer of grease and a rubber disk were used.
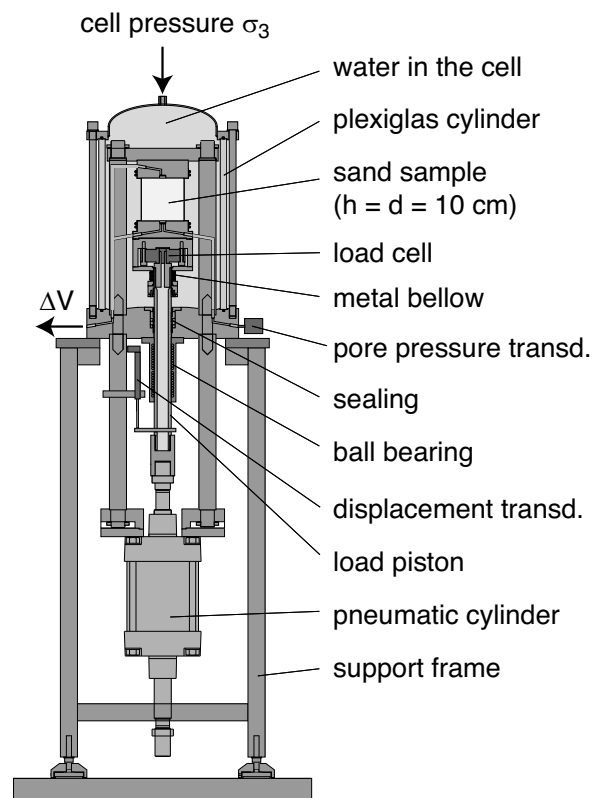
Fig. 6: Scheme of the cyclic triaxial device used for this study
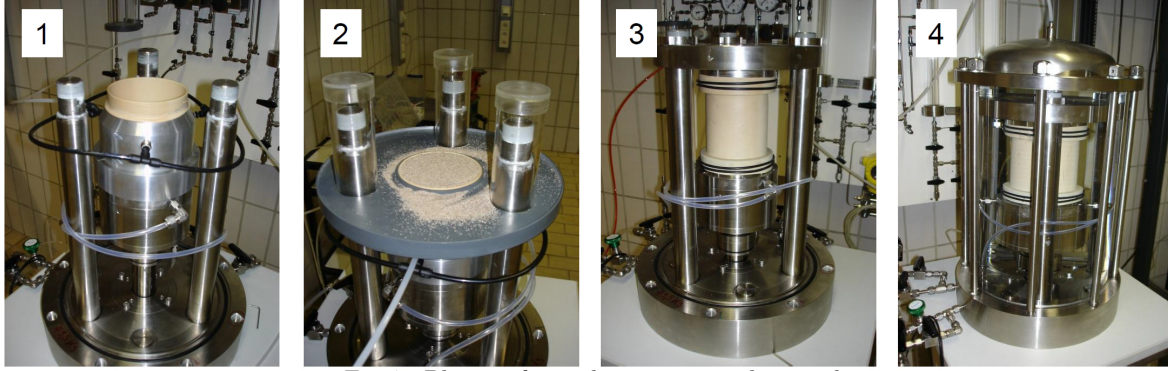
Fig. 7: *Photos of sample preparation by air pluviation*

In the cyclic triaxial device shown in Figure 6 the axial force is measured at a load cell being located directly below the bottom end plate of the sample, i.e. inside the pressure cell. The axial deformation is obtained from a displacement transducer attached to the load piston. The system compliance was determined in preliminary tests on a steel dummy and subtracted from the measured values. Volume changes are determined via the squeezed out pore water using the burette system and a differential pressure transducer (not shown in Figure 6). Two pressure transducers are used for monitoring cell pressure and back pressure.

In the tests of the present series the lateral effective stress has been kept constant ($\sigma'_3 = $ constant), while the vertical effective stress was varied with an amplitude $\sigma_1'^{\text{ampl}}$ around an average value $\sigma_1'^{\text{av}}$ (Figure 8a). The effective stress path is shown schematically in a p-q diagram in Figure 9. After sample preparation by air pluviation, water saturation and a successful B value test, the sample was consolidated for one hour at the average effective stress of the test. This average stress is described by the vertical component $\sigma_1'^{\text{av}}$ and the horizontal component $\sigma_3'^{\text{av}}$ or by the average values of effective mean pressure $p^{\text{av}} = (\sigma_1'^{\text{av}} + 2\sigma_3'^{\text{av}})/3$ and deviatoric stress $q^{\text{av}} = \sigma_1'^{\text{av}} - \sigma_3'^{\text{av}}$, with the average stress ratio defined as $\eta^{\text{av}} = q^{\text{av}}/p^{\text{av}}$. Afterwards the cyclic loading in the axial direction with the amplitude $\sigma_1'^{\text{ampl}}$ was superposed to this average stress. Since the lateral stress was constant during the cycles ($\sigma_3'^{\text{ampl}} = 0$, $\sigma_3' = \sigma_3'^{\text{av}} = $ constant) and the test was performed with open drainage, the resulting effective stress path during the cycles is inclined by 1:3 in the p-q diagram (Figure 9). The amplitudes of deviatoric and vertical stress are identical, i.e. $q^{\text{ampl}} = \sigma_1'^{\text{ampl}}$, while that of mean pressure is $p^{\text{ampl}} = \sigma_1'^{\text{ampl}}/3$.

Due to larger deformations the first *irregular* cycle (Figure 8) was applied with a low loading frequency of 0.01 Hz while a frequency of 0.2 Hz was chosen for the subsequent 10^5 *regular* cycles. The data were continuously recorded during the whole test. From this huge amount of data, the data recorded during the first 24 cycles and during five cycles at $N = 50, 100, 200, 500, \ldots, 5 \cdot 10^4$ and 10^5 were extracted for a further analysis.

For each of the three materials four series of drained cyclic triaxial tests were performed. The stress paths are shown schematically in Figure 10. As reference a test with medium relative density, an average mean pressure $p^{\text{av}} = 200$ kPa and an average stress ratio $\eta^{\text{av}} = 0.75$ has been chosen (i.e. $\sigma_1'^{\text{av}} = 300$ kPa, $\sigma_3'^{\text{av}} = 150$ kPa, thus resulting

in a value $\sigma_3'^{\text{av}}/\sigma_1'^{\text{av}} = 0.5$ being typical for many in situ conditions). The stress amplitude in the reference test has been selected as $q^{\text{ampl}} = \sigma_1'^{\text{ampl}} = 60$ kPa, which leads to strain amplitudes $\varepsilon^{\text{ampl}} \approx 4 \cdot 10^{-4}$ being typical for a high-cyclic loading in real problems. Compared to the reference test, lower or higher deviatoric stress amplitudes q^{ampl} between 20 and 80 kPa were applied in the first series of tests (Figure 10a). All other boundary conditions (density, average stress) were chosen as in the reference test. In the second series, the initial relative density I_{D0} was varied between medium dense and dense, keeping the average and cyclic stresses identical to the reference test (Figure 10b). For each material three or four different densities were tested. Four or five different average mean pressures in the range 50 kPa $\leq p^{\text{av}} \leq$ 300 kPa were examined in the third series (Figure 10c), while the density, the average stress ratio $\eta^{\text{av}} = 0.75$ and the amplitude-pressure ratio $\zeta = q^{\text{ampl}}/p^{\text{av}} = 0.3$ were the same as in the reference test. Finally, in the fourth test series (Figure 10d) the average stress ratio η^{av} was varied between 0.0 and 1.25, keeping density, p^{av} and q^{ampl} as in the reference test. Four or five tests with different η^{av} values were conducted for each material. Each of these tests was performed on a fresh sample, i.e. no multistage testing was done.

Note, that the initial relative density $I_{D0} = (e_{\max} - e_0)/(e_{\max} - e_{\min})$ given herein is calculated with the void ratio e_0 measured at the average mean pressure p^{av} prior to the start of the regular cycles. A value $I_{D0} = 1.18$ was obtained in one of the tests on the crushed sand. In principle, relative densities larger than 1.0 are possible due to two different reasons: First, it has to be considered that $e_{\min}$ and $e_{\max}$ are determined from standardized testing procedures. By certain sample preparation techniques like air pluviation using a funnel with a very small outlet diameter one can reach void ratios slightly below $e_{\min}$. Second, a void ratio $e_0 < e_{\min}$ can be reached during the increase of pressure to p^{av}, in particular in case of a high compressibility of the grain skeleton as observed for the angular crushed sand. Additionally, also cyclic loading may cause a compaction resulting in $e < e_{\min}$ after a large number of cycles [96].

Figure 11 presents data recorded during the first 24 regular cycles of three tests on the natural sand with the reference stress conditions ($p^{\text{av}} = 200$ kPa, $\eta^{\text{av}} = 0.75$, $q^{\text{ampl}} = 60$ kPa) and different initial relative densities I_{D0}. The diagrams show the relationships between deviatoric stress q and axial strain ε_1 or volumetric strain ε_v, respectively, and the curves of void ratio change $e - e_0$ versus effective
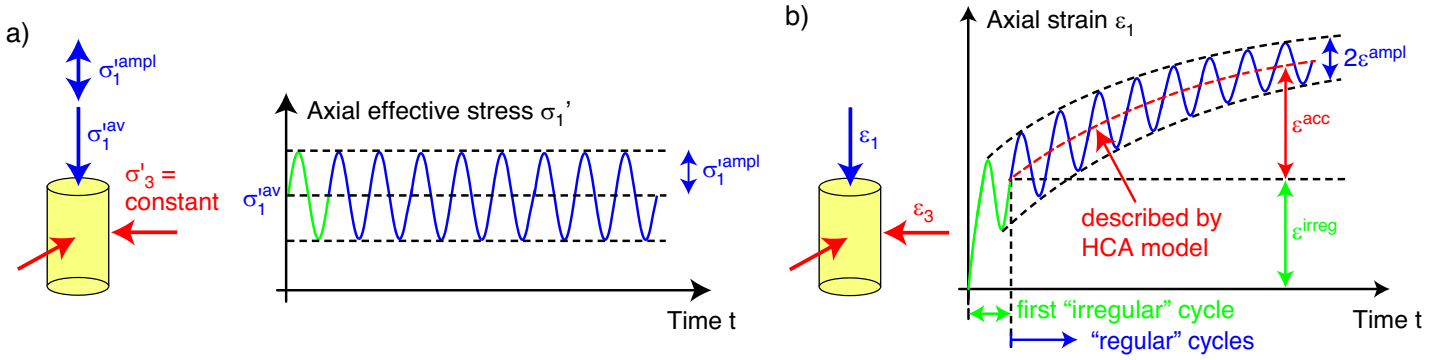
Fig. 8: a) Axial effective stress σ_1' and b) axial strain ε_1 versus time in a drained cyclic triaxial test
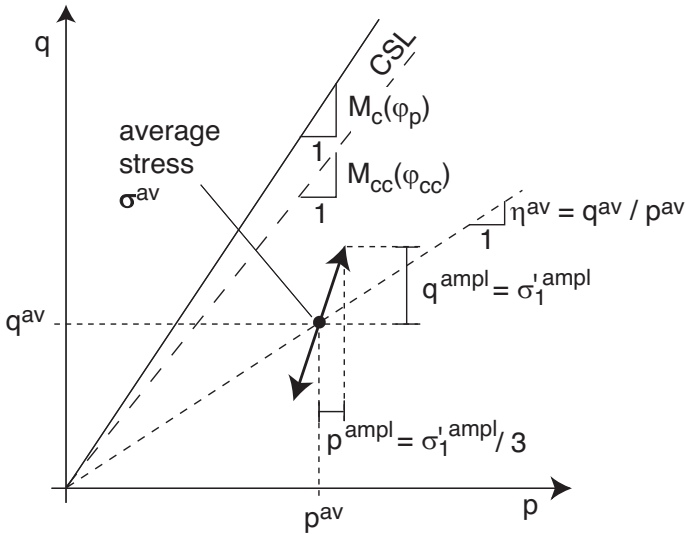
Fig. 9: Stress path in a cyclic triaxial test shown in the p-q diagram

mean pressure p. The accumulation of axial and volumetric strain and the associated reduction of void ratio are obvious in these representations. The lower the density, the larger is the accumulated strain or void ratio change per cycle.

Since the HCA model predicts the strain accumulation rates due to the regular cycles only, the first irregular cycle is not discussed in this paper. In the following, $N = 1$ thus refers to the end of the first regular cycle (Figure 8). In the HCA model of Niemunis et al. [51] the tensor of the rate of strain accumulation is described by $\dot{\boldsymbol{\varepsilon}}^{\mathrm{acc}} = \dot{\varepsilon}^{\mathrm{acc}}\mathbf{m}$, i.e. as the product of the scalar *intensity* of accumulation $\dot{\varepsilon}^{\mathrm{acc}} = \|\dot{\boldsymbol{\varepsilon}}^{\mathrm{acc}}\|$ (norm of strain rate tensor) and the *direction* of accumulation $\mathbf{m} = \dot{\boldsymbol{\varepsilon}}^{\mathrm{acc}}/\|\dot{\boldsymbol{\varepsilon}}^{\mathrm{acc}}\|$ (unit tensor, see Appendix). In the triaxial case, the intensity of accumulation is calculated as $\dot{\varepsilon}^{\mathrm{acc}} = \sqrt{(\dot{\varepsilon}_1^{\mathrm{acc}})^2 + 2(\dot{\varepsilon}_3^{\mathrm{acc}})^2}$ with the rates of axial and radial strain accumulation. The direction of accumulation can be expressed by the ratio of the volumetric and deviatoric strain accumulation rates $\omega = \sqrt{3/2}\,\mathrm{tr}\,(\mathbf{m})/\|\mathbf{m}^*\| = \dot{\varepsilon}_v^{\mathrm{acc}}/\dot{\varepsilon}_q^{\mathrm{acc}}$ with $\dot{\varepsilon}_v^{\mathrm{acc}} = \dot{\varepsilon}_1^{\mathrm{acc}} + 2\dot{\varepsilon}_3^{\mathrm{acc}}$ and $\dot{\varepsilon}_q^{\mathrm{acc}} = 2/3(\dot{\varepsilon}_1^{\mathrm{acc}} - \dot{\varepsilon}_3^{\mathrm{acc}})$. In the following, the test results are first analysed regarding the direction of accumulation and then with respect to its intensity.

4.2 Direction of accumulation - high-cyclic flow rule m

Figure 12 presents the accumulated deviatoric strain $\varepsilon_q^{\mathrm{acc}}$ as a function of the accumulated volumetric strain $\varepsilon_v^{\mathrm{acc}}$ measured in selected tests. Each data point in those diagrams refers to a certain number of cycles ($N = 1, 2, 5, 10, \ldots, 10^5$). For all three materials, the direction of the $\varepsilon_q^{\mathrm{acc}}$-$\varepsilon_v^{\mathrm{acc}}$ strain paths was found to be rather independent of stress amplitude, density and average mean pressure (see the diagrams for crushed sand in Figure 12a-c). For all three materials, the average stress ratio η^{av} is the governing parameter for the direction of accumulation (Figure 12d-f). The larger η^{av} the larger is the deviatoric component of the strain accumulation rate, i.e. the lower is the ratio $\dot{\varepsilon}_v^{\mathrm{acc}}/\dot{\varepsilon}_q^{\mathrm{acc}}$. The dependence of the strain rate ratio on η^{av} can be well described by the following equation adopted from the flow rule of the Modified Cam clay model:

$$\frac{\dot{\varepsilon}_v^{\mathrm{acc}}}{\dot{\varepsilon}_q^{\mathrm{acc}}} = \frac{M_{cc}^2 - (\eta^{\mathrm{av}})^2}{2\eta^{\mathrm{av}}} \tag{1}$$

with $M_{cc} = \dfrac{6\sin\varphi_{cc}}{3 - \sin\varphi_{cc}}$ for triaxial compression tests. Eq. (1) means that the strain accumulation is purely volumetric ($\dot{\varepsilon}_q^{\mathrm{acc}} = 0$) at $\eta^{\mathrm{av}} = 0$ and purely deviatoric ($\dot{\varepsilon}_v^{\mathrm{acc}} = 0$) at $\eta^{\mathrm{av}} = M_{cc}$, i.e. at an average stress ratio corresponding to the critical friction angle φ_{cc}. The φ_{cc} and corresponding M_{cc} values delivering the optimum approximation of the cyclic test data are summarized in Table 2. The $\varepsilon_q^{\mathrm{acc}}$-$\varepsilon_v^{\mathrm{acc}}$ strain paths predicted by Eq. (1) with these φ_{cc} values have been added as thick solid lines in Figure 12d-f. The data in Table 2 reveals that φ_{cc} significantly increases with increasing angularity of the grains. This is in accordance with the higher peak friction angles φ_P observed in the drained monotonic tests (Section 3) and can be again explained by an increased interparticle friction and interlocking. Consequently, at a certain average stress ratio η^{av} the ratio of volumetric and deviatoric strain accumulation rate is higher for a more angular material, due to the larger distance of the average stress to the critical state line in the p-q plane.

For comparison, the angles of repose φ_r obtained as the inclination of a pluviated cone of sand and the corresponding M_r values are also provided in Table 2. Obviously, for all three tested materials the φ_{cc} and φ_r values agree well. This corroborates the recommendation for natural sands in [93] that φ_{cc} can be estimated from the relationship $\varphi_{cc} \approx \varphi_r$ in the absence of cyclic test data. Based on the present test data such simplified calibration seems feasible irrespective

Fig. 10: *Stress paths in the four series of cyclic tests performed on each material shown in the p-q diagram*
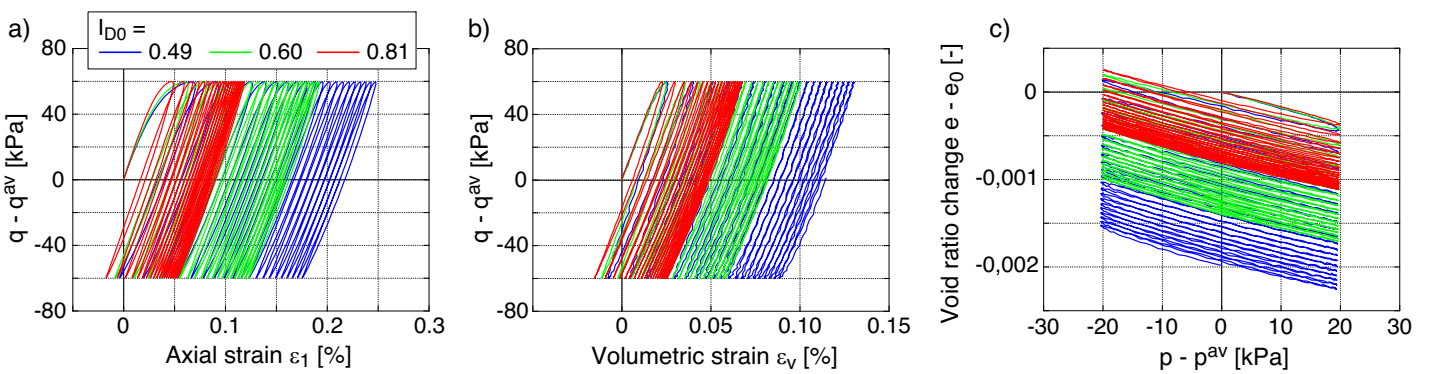
Fig. 11: *Data during the first 24 cycles of three tests on the natural sand with the reference stress conditions ($p^{av} = 200$ kPa, $\eta^{av} = 0.75$, $q^{ampl} = 60$ kPa) and different initial relative densities I_{D0}: a) Deviatoric stress $q - q^{av}$ versus axial strain ε_1, b) Deviatoric stress $q - q^{av}$ versus volumetric strain ε_v, c) Void ratio change $e - e_0$ versus effective mean pressure $p - p^{av}$*
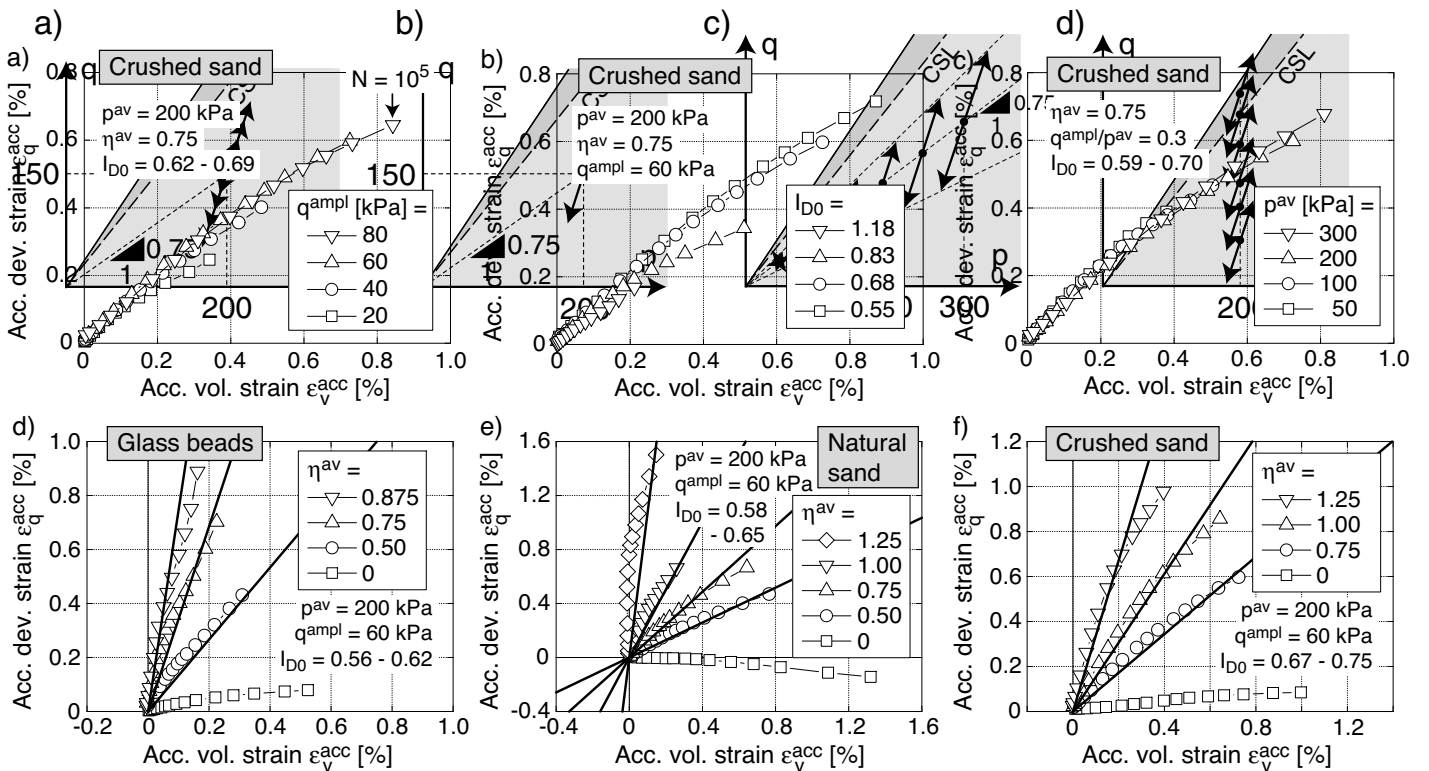
Fig. 12: *ε_q^{acc}-ε_v^{acc} strain paths measured a)-c) for crushed sand in tests with different stress amplitudes, densities and average mean pressures and d)-f) for glass beads, natural sand and crushed sand in tests with different average stress ratios. The solid lines in diagrams d)-f) have been generated using Eq. (1) with the φ_{cc} values in Table 2.*

4.3 Intensity of accumulation

The curves of accumulated strain $\varepsilon^{\mathrm{acc}}$ versus the number of cycles N measured for the three different test materials in the four different test series are provided in Figure 13. The curves obtained for the crushed sand run almost proportional to $\ln(N)$ up to the maximum number of cycles applied in the tests ($N = 10^5$). Most of the data collected for the natural sand and the glass beads obey $\varepsilon^{\mathrm{acc}}(N) \sim \ln(N)$ only up to $N = 10^4$. At larger number of cycles the residual strain increases faster than logarithmic with the number of cycles, i.e. the inclination of the curves in the $\varepsilon^{\mathrm{acc}}$-$N$ diagrams with semi-logarithmic scale increases. The test data in Figure 13 reveal that beside the grain size distribution curve [94,97] also the grain characteristics influence the shape of the strain accumulation curves $\varepsilon^{\mathrm{acc}}(N)$. The stronger decay of the rate of strain accumulation with increasing number of cycles observed for the more angular materials, in particular at $N > 10^4$, may be again a result of the interlocking between the particles, that increases due to the small rearrangements of the grains during cyclic loading and restraints further particle mobility.

For all three materials, the intensity of strain accumulation grows with increasing values of amplitude (Figure 13a-c) and stress ratio (Figure 13j-l) while it decreases if the sand becomes denser (Figure 13d-f). In case of the natural sand, the strain accumulation curves measured for the different average mean pressures are similar if the amplitude-pressure ratio $q^{\mathrm{ampl}}/p^{\mathrm{av}}$ is chosen identical in all tests (Figure 13h). For both other tested materials, however, the residual strains were found either to decrease (glass beads, Figure 13g) or increase (crushed sand, Figure 13i) with growing pressure. This is a result of the differences in the pressure-dependence of the cumulative rates discussed in the following.

Figure 14 compares the accumulated strains $\varepsilon^{\mathrm{acc}}$ of the three different materials after $N = 10^5$ cycles. The data are plotted as functions of the parameters q^{ampl}, I_{D0}, p^{av} and $\eta^{\mathrm{av}}/M_{cc}$ (normalized average stress ratio) varied in the four test series. While for glass beads and natural sand the residual strain grows approximately according to a square function with increasing stress amplitude, it increases slightly lower than proportional ($\varepsilon^{\mathrm{acc}} \sim q^{\mathrm{ampl}}$) in case of the crushed sand (Figure 14a). With increasing stress and strain amplitude, particle rearrangements due to rolling and sliding are facilitated in the materials with more rounded grains, while they are restraint by interlocking in case of more angular particles.

The largest differences are obvious in the tests with different average mean pressures (Figure 14c). The tests on glass beads showed a significant decrease of the residual strain with increasing values of p^{av}. Also the natural sand exhibited a moderate decrease while the opposite tendency was observed for the crushed sand. At low pressures ($p^{\mathrm{av}} = 50$ kPa) the intensity of strain accumulation was higher in the glass beads than in the natural sand and in particular in the crushed sand (in accordance with undrained cyclic tests [1,34,80]). At higher pressures ($p^{\mathrm{av}} = 300$ kPa), however, no significant differences between the residual strains measured for the three different materials could be detected. It should be noted that in the tests with $p^{\mathrm{av}} = 300$ kPa the initial density was the same ($I_{D0} = 0.56$) for glass

beads and natural sand, but somewhat higher ($I_{D0} = 0.70$) for the crushed sand, owed to the higher compressibility of the latter material during pressure increase. If the crushed sand was tested at $I_{D0} = 0.56$ too, then probably a somewhat higher residual strain was observed, i.e. the point for the crushed sand would lie slightly above those for the two other materials in Figure 14c.

A possible explanation for the tendencies in Figure 14c may be given based on micromechanics. Considering two particles in contact, a contact force generates elastic deformations of the contact zone, as originally demonstrated by Hertz [25] for the contact of two spheres. Goddard [19] derived analogous formulas for a contact of a cone and a sphere, which comes closer to the contact characteristics of reals soils. Goddard [19] demonstrated, that when exceeding a certain stress level acting on the grain packing, the contact of a cone and a sphere behaves similar to a contact of two spheres, i.e. a Hertz contact. Thus, at elevated stresses the original shape of the contact does not affect the contact behaviour anymore. According to Goddard [19] the transition stress depends on the grain material and the angle of the cone, but it lies well below the pressures causing grain breakage, i.e. in the range of pressures typically applied in triaxial tests on sands. Furthermore, studies with uniaxial compression tests on single grains [7] have shown that plastic deformations of contacts can occur already at low contact stresses, due to a plastification or damage of asperities. The plastic deformations can be explained by the fact that at low stresses applied to the grain skeleton and in particular in case of angular particles, the initial contact area between two particles is very small. Therefore, the stresses in the contact zone may be large even if the contact force is low. Based on these considerations it can be assumed that an increase in pressure will lead to both elastic and plastic deformations at the grain contacts, and that with increasing pressure applied to a specimen, the original shape of the particles involved in the contacts becomes less important regarding the behaviour of the contacts and thus the response of the whole granular packing. This leads to a similar cumulative response of the materials with different grain shape at elevated pressures. At lower stress levels, reorientations of the particles due to sliding and rotation are easier in the assemblies of round glass beads with their smooth surface than in the angular crushed sand with a higher interparticle friction and a distinct interlocking between adjacent grains.

A similar tendency for the liquefaction resistance of materials with different grain shape is reported in [80]. In [80], however, even larger pressures up to 800 kPa have been tested and the observations have been partly attributed to particle breakage effects. In contrast, no noticeable particle breakage has been detected in the present study (Section 5).

The relationship between residual strain and relative density (Figure 14b) is similar for glass beads and natural sand, while the decrease of $\varepsilon^{\mathrm{acc}}$ with I_{D0} is somewhat weaker for the crushed sand. Also the dependence of residual strain on normalized stress ratio $\eta^{\mathrm{av}}/M_{cc}$ seems to get slightly less pronounced when the angularity of the particles increases (Figure 14d). Generally, the higher interparticle friction and the interlocking between adjacent particles in case of an angular grain shape seems to weaken the dependencies of the strain accumulation rate on stress or strain
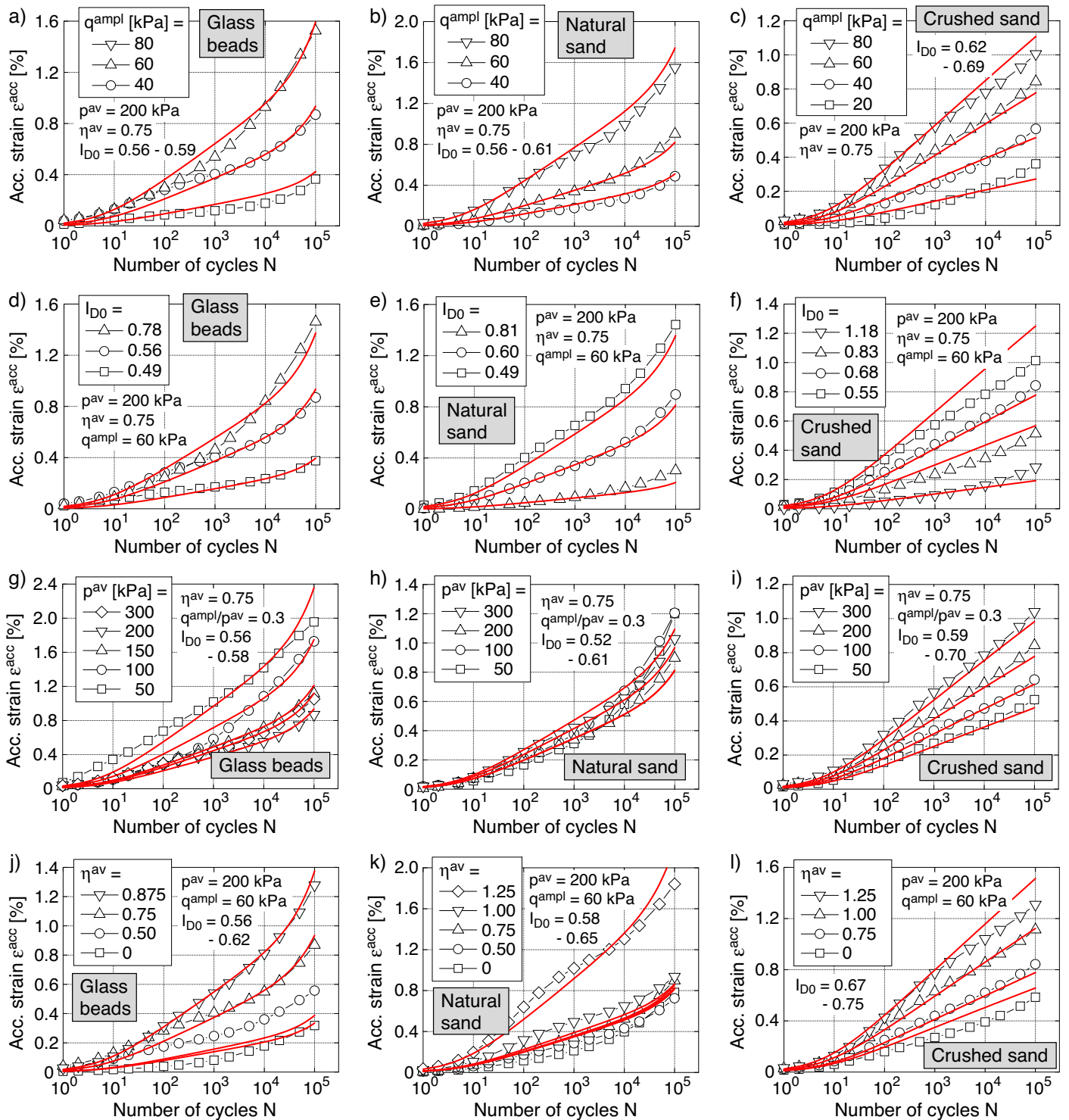
Fig. 13: Strain accumulation curves $\varepsilon^{acc}(N)$ measured for glass beads (1st column), natural sand (2nd column) and crushed sand (3rd column) in the four test series with a variation of stress amplitude (first row), initial relative density (second row), average mean pressure (third row) and average stress ratio (fourth row). The red curves stem from simulations of the tests with the HCA model using the optimum parameters in Table 2

Material	φ_{cc} [°]	φ_r [°]	M_{cc} [-]	M_r [-]	C_{ampl} [-]	C_e [-]	C_{p1} [-]	C_{p2} [-]	C_Y [-]	C_{N1} [10^{-4}]	C_{N2} [-]	C_{N3} [10^{-5}]
Glass beads	24.9	25.4	0.98	1.00	2.15	0.50	0.25	2.46	2.73	1.20	0.17	3.5
Natural sand	32.8	33.2	1.32	1.34	1.80	0.56	0	0.30	2.20	2.80	0.18	3.0
Crushed sand	37.3	37.3	1.52	1.52	0.95	0.48	0	-0.19	2.33	2.50	0.15	0

Table 2: Critical friction angles φ_{cc} derived from the cyclic test data, angles of repose φ_r obtained from the inclination of a pluviated cone of sand, corresponding inclinations M_{cc} and M_r and HCA model parameters used in the equations for the intensity of accumulation for the three tested materials
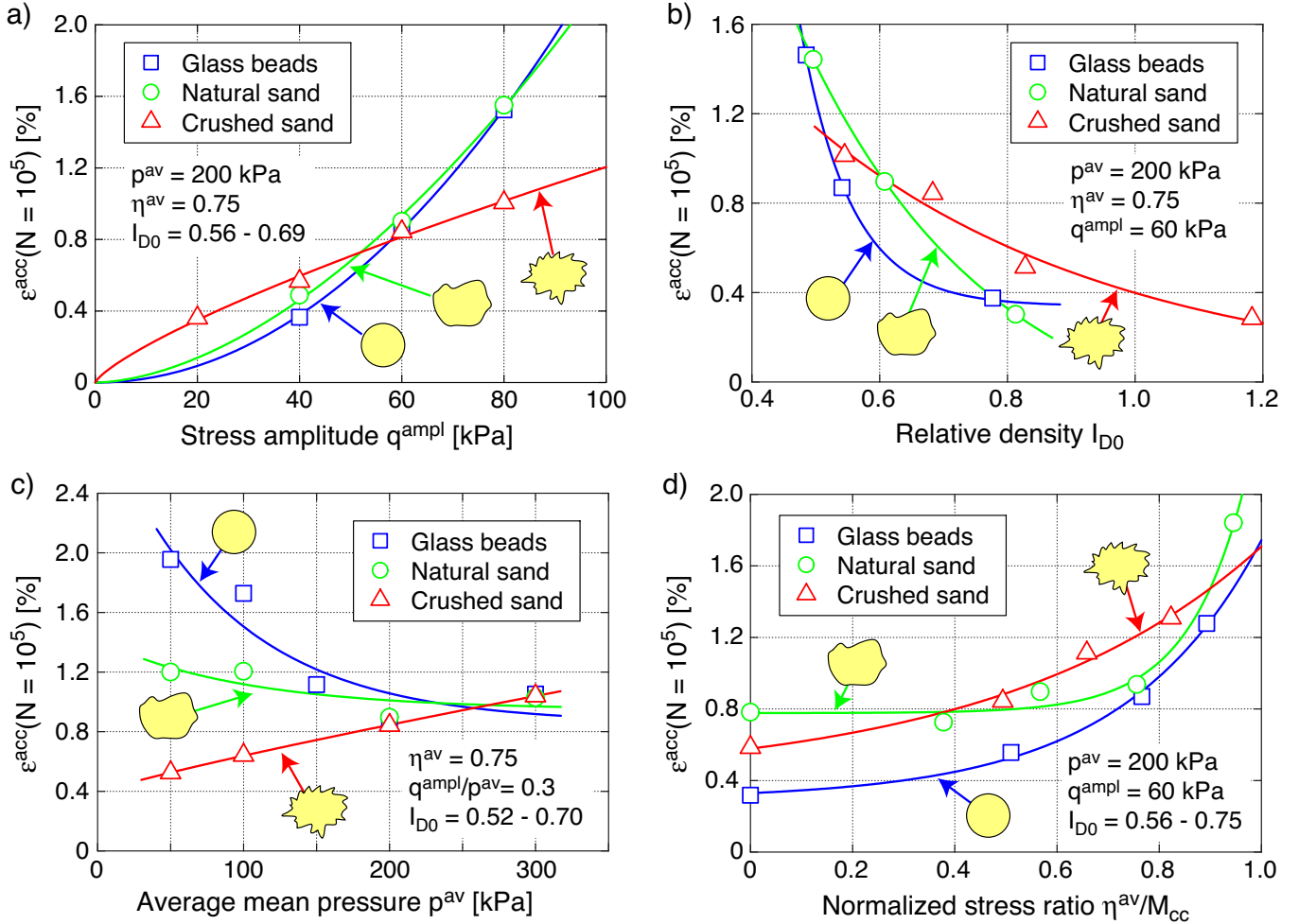
Fig. 14: Accumulated strain ε^{acc} after $N = 10^5$ cycles as a function of a) stress amplitude q^{ampl}, b) initial relative density I_{D0}, c) average mean pressure p^{av} and d) normalized average stress ratio η^{av}/M_{cc}

amplitude, relative density and average stress ratio.

In a similar manner, the elastic portion of strain is analyzed in Figure 15. In those diagrams mean values of the strain amplitude during 10^5 cycles are plotted versus the four varied parameters. As expected and in accordance with earlier work [88, 94], for all three test materials the strain amplitude grows with increasing stress amplitude, decreasing density, increasing pressure (for $\zeta = q^{ampl}/p_0 =$ constant) and decreasing stress ratio. For all test conditions the strain amplitudes measured for the crushed sand exceeded those observed for the two other materials. The elastic strains for the glass beads and the natural sand were quite similar. Analogously to the stiffness E_{50} in the monotonic tests (Section 3), the larger strain amplitudes and thus lower values of secant stiffness in case of the crushed

sand can be partially attributed to the higher void ratios and lower coordination numbers at same relative density. Furthermore, the stiffness at small to moderate strains reflects the nature of interparticle contacts. Below the transition pressure, contacts between angular particles are more deformable, as can be readily shown by comparing a cone-to-plane contact [19] versus a sphere-to-plane contact [25], cf. [9].

4.4 HCA model parameters

In order to calibrate the HCA model for the three different test materials (the procedure is explained in detail in [89] and [83]) the diagrams provided in Figure 16 have been generated. The first row of diagrams shows the residual strain ε^{acc} as a function of the strain amplitude $\bar{\varepsilon}^{ampl}$ for different
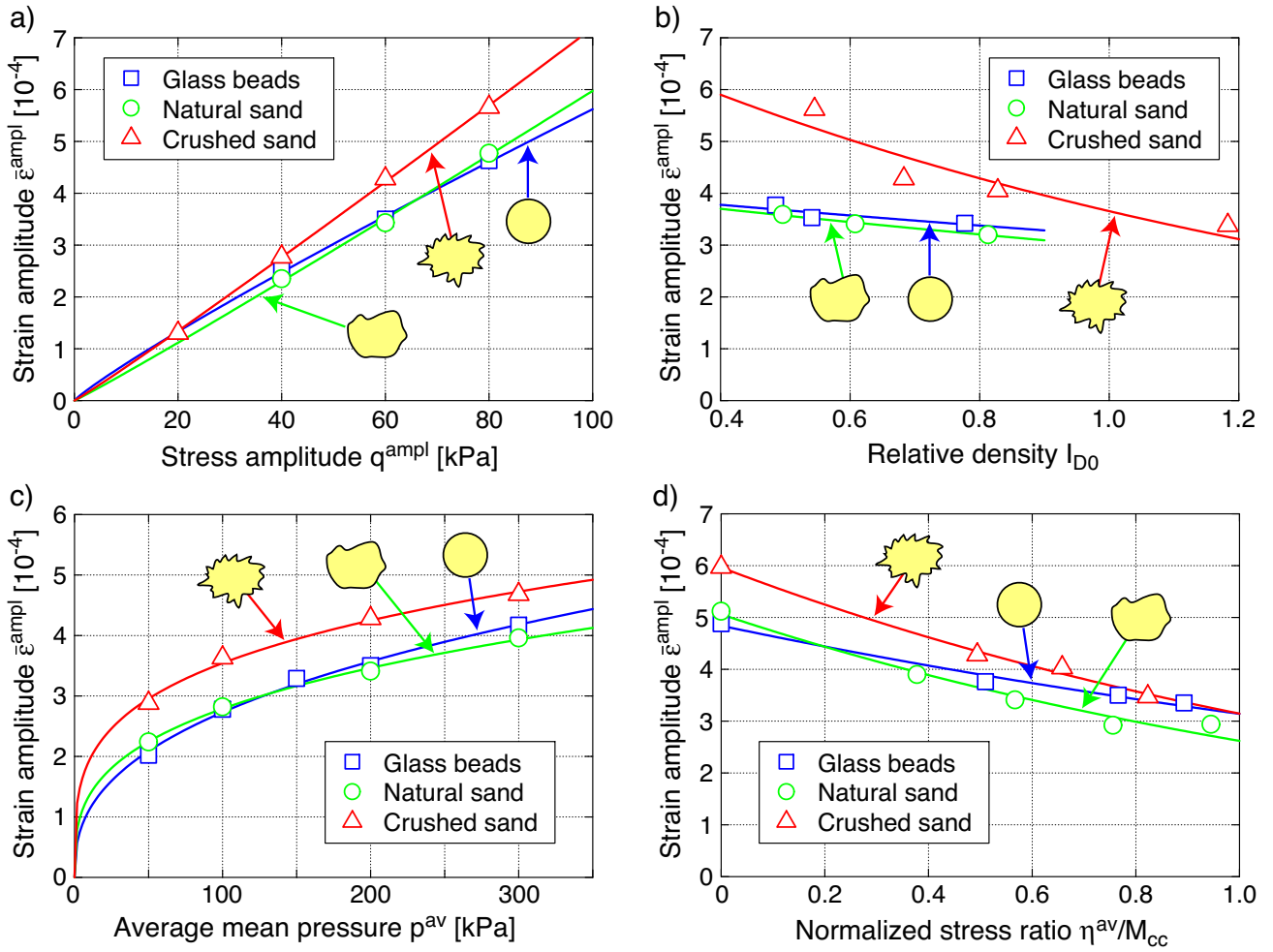
Fig. 15: *Strain amplitude $\bar{\varepsilon}^{ampl}$ (mean values over 10^5 cycles) as a function of a) stress amplitude q^{ampl}, b) initial relative density I_{D0}, c) average mean pressure p^{av} and d) normalized average stress ratio η^{av}/M_{cc}*

numbers of cycles. Since the tests have been performed with stress cycles, the strain amplitude slightly varies (usually decreases) with increasing number of cycles. The strain amplitude $\bar{\varepsilon}^{ampl}$ is a mean value up to the N value under consideration. On the ordinate the ε^{acc} data have been divided by the void ratio function $\bar{f}_e$ of the HCA model (see Table 3 in Appendix) in order to eliminate the influence of slightly different initial densities and the higher compaction rates $\dot{e} = \partial e/\partial N$ in the tests with larger stress amplitudes. The void ratio $\bar{e}$ entering the void ratio function is also a mean value over the N previously applied cycles. A comparison of the diagrams in Figure 16a-c reveals that the increase of the residual strain $\varepsilon^{acc}/\bar{f}_e$ with increasing strain amplitude $\bar{\varepsilon}^{ampl}$ is more pronounced for the glass beads than for the natural sand. In agreement with Figure 14a, in case of the crushed sand at large numbers of cycles the residual strain grows even slower than linear with increasing strain amplitude. The parameters C_{ampl} of the amplitude function f_{ampl} (Appendix, Table 3) have been gathered from the diagrams in Figure 16a-c by fitting the function $f = k \, (\bar{\varepsilon}^{ampl})^{C_{ampl}}$ to the data for each N value (solid curves in Figure 16a-c), resulting in the parameter C_{ampl} and a constant k which is not used further. The mean value of the parameters collected for the different numbers of cycles has been chosen as C_{ampl} (the C_{ampl} value given in Table 2 results from a

further optimization as explained below).

The second row of diagrams in Figure 16 contains the data from the test series with a variation of initial density. In those diagrams the residual strain has been plotted versus void ratio $\bar{e}$. The residual strain has been divided by the amplitude function $\bar{f}_{ampl}$ of the HCA model with the aim to eliminate the effect of the moderately different strain amplitudes $\bar{\varepsilon}^{ampl}$ (Figure 15b). The increase of the residual strain with increasing void ratio looks similar for all three tested materials. The HCA model parameter C_e of the void ratio function f_e, corresponding to the void ratio for which $\dot{\varepsilon}^{acc} = 0$ holds, was obtained by fitting the function $f = k \, (C_e - e)^2/(1+e)$ to the data for each number of cycles in Figure 16d-f (solid curves). While the parameter k is not further used, the C_e values derived for the various N values have been finally averaged. Since the function $\bar{f}_e$ with the parameter C_e is necessary on the ordinate of the diagrams in Figure 16a-c and the function $\bar{f}_{ampl}$ with its parameter C_{ampl} is used in the diagrams in Figure 16d-f, the simultaneous determination of the material constants C_{ampl} and C_e has to be done by iteration. As a first estimate for C_e, the correlation $C_e = 0.95 e_{min}$ can be applied. With this value for C_e, the first determination of C_{ampl} is conducted. This C_{ampl} value is used in the first curve-fitting for C_e. With the obtained C_e the determination of C_{ampl}

11

is refined, and so on. Usually two or three iterations are sufficient to obtain the final values of C_{ampl} and C_e. The solid curves shown in Figure 16a-c and 16d-f stem from the last iteration. C_e corresponds to the void ratio where the curves in the diagrams in Figure 16d-f would intersect the ordinate.

The third row of diagrams in Figure 16 analyzes the pressure-dependence of the strain accumulation rate. The residual strain has been divided by $\bar{f}_{\mathrm{ampl}}$ and $\bar{f}_e$ in order to purify it from the influences of strain amplitude (Figure 15c) and void ratio. In contrast to Figure 14c, the data in Figure 16g-i thus refers to a constant strain amplitude. The data reveal that the decrease of the strain accumulation rate with increasing pressure is much more pronounced for the glass beads than for the natural sand. For crushed sand, the relationship is the other way around, i.e. $\dot{\varepsilon}^{\mathrm{acc}}$ slightly increases with increasing pressure. The data for the glass beads in Figure 16g could not be fitted sufficiently well by the original function f_p of the HCA model (Appendix, Table 3, for the fitting the parameter k is again set in front of f_p). Thus, the function was extended by a constant portion according to:

$$f_p = C_{p1} + (1 - C_{p1}) \exp[-C_{p2}(p^{\mathrm{av}}/100 - 1)] \quad (2)$$

with two parameters C_{p1} and C_{p2}. For $C_{p1} = 0$ the original function is regained with $C_p = C_{p2}$. In accordance with the original function, also the modified f_p according to Eq. (2) delivers $f_p = 1$ at the reference pressure $p^{\mathrm{av}} = 100$ kPa. In case of the natural sand and the crushed sand the original function was sufficient to approximate the data in Figure 16h,i and thus $C_{p1} = 0$ holds for these two materials. The increasing trend of $\dot{\varepsilon}^{\mathrm{acc}}$ with p^{av} observed for the crushed sand results in a negative C_{p2} value. The procedure of curve-fitting to obtain C_{p1} and C_{p2} is identical to that in case of C_{ampl} and C_e, but no iterative procedure is necessary. The final C_{pi} values result from an averaging of the individual C_{pi} values determined for the various numbers of cycles.

The last row of diagrams in Figure 16 has been used to determine the parameter C_Y in the stress ratio function f_Y of the HCA model (Appendix, Table 3). The residual strain divided by the void ratio and amplitude functions is plotted versus the normalized average stress ratio $\bar{Y}^{\mathrm{av}}$ ($\bar{Y}^{\mathrm{av}} = 0$ for $\eta^{\mathrm{av}} = 0$ and $\bar{Y}^{\mathrm{av}} = 1$ for $\eta^{\mathrm{av}} = M_{cc}$, see Appendix). A fitting of the function $k\,f_Y$ to the data in those diagrams delivered C_Y.

Afterwards an element test program has been used in order to determine the parameters C_{N1}, C_{N2} and C_{N3} describing the increase of the residual strain with increasing number of cycles (Appendix, Table 3) and in order to optimize the parameters C_{ampl}, C_e, C_{p1}, C_{p2} and C_Y. All cyclic tests performed in this study have been simulated with the element test program. The parameters derived from the diagrams in Figure 16 were used as the starting point. The parameters have been varied in consecutive simulations until the best congruence between the measured and the predicted curves $\varepsilon^{\mathrm{acc}}(N)$ had been achieved. The optimum HCA model parameters are summarized in Table 2. The $\varepsilon^{\mathrm{acc}}(N)$ curves predicted by the HCA model with these parameters have been added as red solid lines in Figure 13, confirming a good agreement between measured and calculated data for most tests.

Finally, the HCA model parameters are plotted versus the grain shape parameters Circularity and Aspect Ratio

(Table 1) in Figure 17. The exponent C_{ampl} of the amplitude function increases with increasing Circularity or decreasing Aspect Ratio of the grains (Figure 17a,b). No clear dependence of C_e on the grain shape parameters can be detected in Figure 17c,d. The parameters C_{p2} in Figure 17e,f and C_Y in Figure 17g,h exhibit an increase with increasing Circularity and decreasing Aspect Ratio. No diagram for C_{p1} is provided in Figure 17 since only one data point unequal zero is available yet. While C_{N1} is lower for higher values of Circularity and lower values of Aspect Ratio (Figure 17i,j), no clear trend can be observed for C_{N2} (Figure 17k-l) and the opposite relationship is obtained for C_{N3} (Figure 17m-n). Note that the parameter C_{N3} could be better judged based on tests with even higher numbers of cycles ($N \geq 10^6$) [97]. Summing up, Figure 17 demonstrates that several HCA model parameters strongly depend on grain shape.

5 Remarks on grain crushing

Grain crushing or particle abrasion have not been explicitly investigated in the present study. However, they would lead to a certain amount of fines in the mixture at the end of a test, which has not been observed in the present experiments.

Another series of drained cyclic tests with similar ranges of relative densities and stresses (i.e. stress paths as shown in Figure 10) has been recently performed by the authors on a carbonate sand from The Philippines, composed of grains being more susceptible to crushing than the quartz particles tested in the present study. A possible grain crushing was quantified by accurate sieve analyses of the whole triaxial sample once before and once after a test with 10^5 cycles. A comparison of the grain size distribution curves before and after a test (as recommended by Hardin [24] to evaluate the relative breakage ratio B_r) did show only a very small increase of the amount of fines. The low amount of particle breakage is probably due to the moderate average and cyclic stresses applied in the tests. Based on this test series no significant particle breakage or abrasion may be expected for the quartz grains tested in the present study.

Sands with crushable particles like carbonate sands are often composed of grains with a rather angular or irregular shape. Therefore, the material response under monotonic or cyclic loading is influenced by both the crushability and the particle shape simultaneously. It could be expected that crushable sands show larger cumulative rates, not only because of particle breakage but also attributed to higher void ratios and thus larger compressibility typically observed for such granular materials. However, several studies in the literature with undrained cyclic loading have found the opposite tendency. Crushable sands do not liquefy as easily as harder-grained sands of same density (e.g. [15, 26, 27, 41, 61, 62]), primarily due to interlocking effects resulting from the more angular particle shape, rendering the fabric more stable against undrained cyclic loading. The opposite behaviour, i.e. a higher liquefaction susceptibility for crushable sands compared to harder-grained materials has been, however, sometimes observed at higher densities and larger stresses [27, 61]. The latter may be partly attributed to the larger amount of particle breakage occurring at elevated pressure levels.

Some studies on calcareous sands in the literature (e.g. [15]) report a considerable amount of breakage of parti-
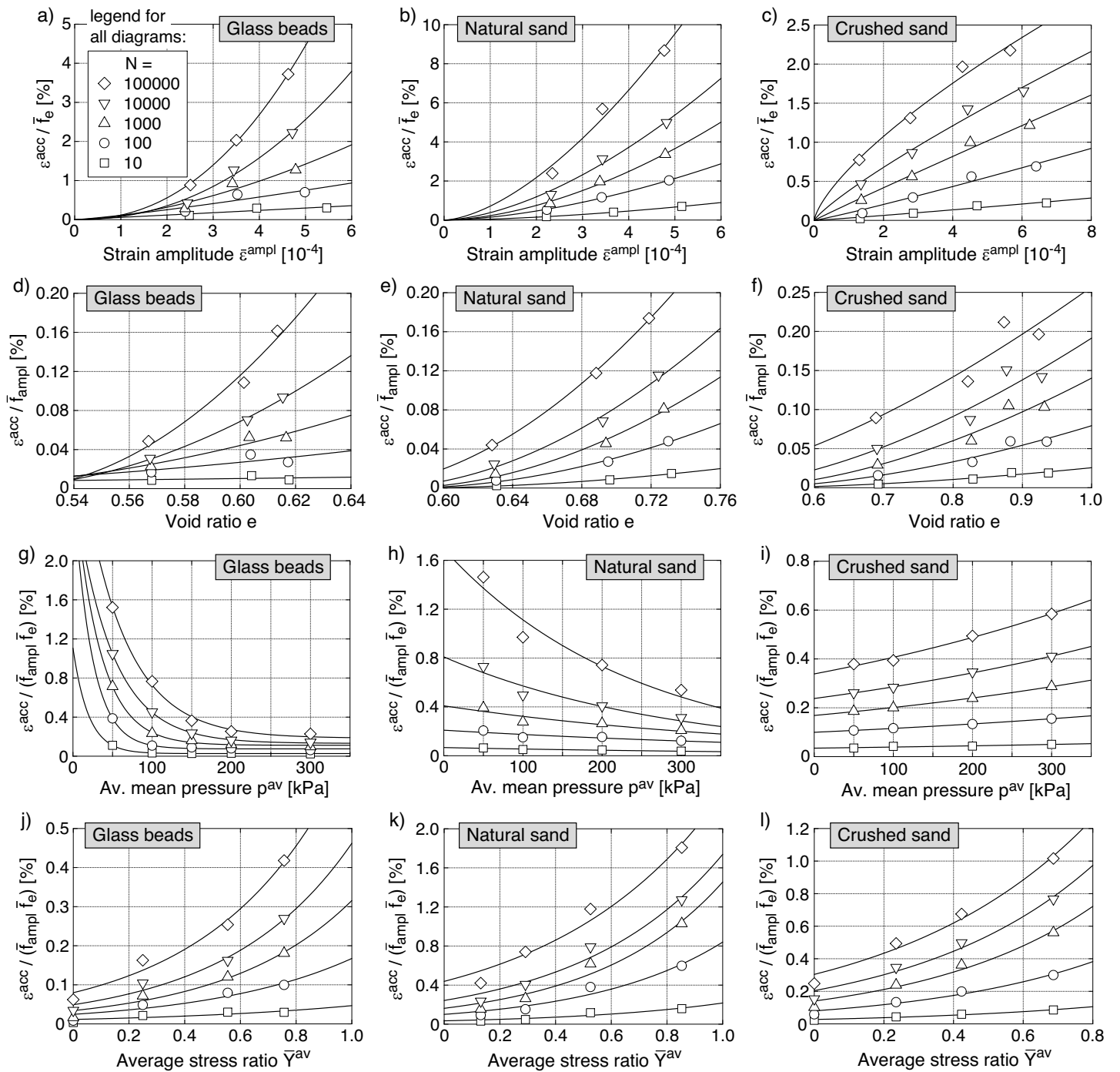
Fig. 16: *Accumulated strain (normalized with f_e and/or f_{ampl} to purify the data from the influences of void ratio and/or amplitude, respectively) versus a) strain amplitude $\bar{\varepsilon}^{ampl}$ (mean value up to cycle number N under consideration), b) void ratio $\bar{e}$ (mean value up to cycle number N), c) average mean pressure p^{av} and d) normalized average stress ratio $\bar{Y}^{av}$ ($\bar{Y}^{av} = 0$ for $\eta^{av} = 0$ and $\bar{Y}^{av} = 1$ for $\eta^{av} = M_{cc}$)*
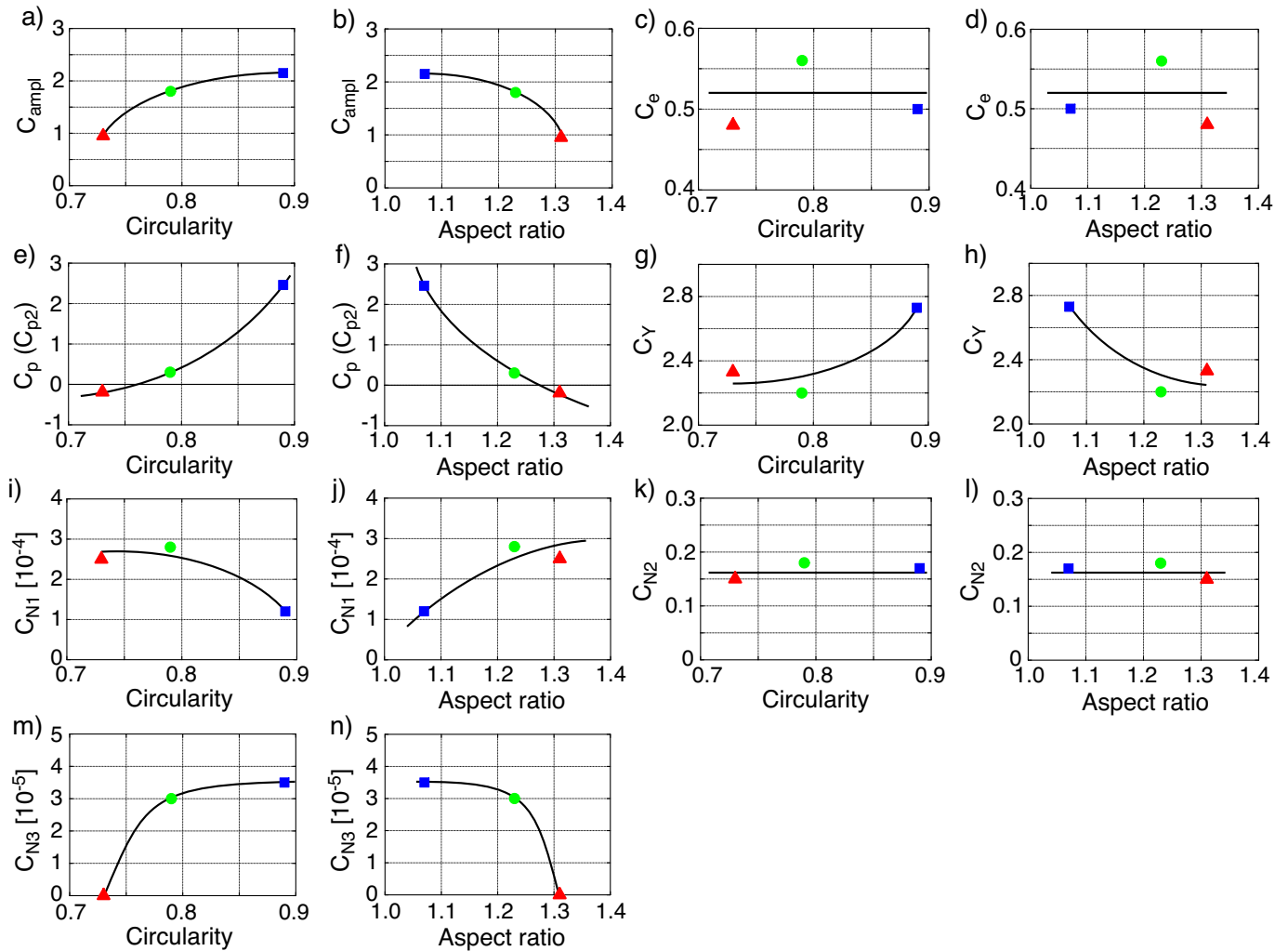
Fig. 17: *HCA model parameters as a function of grain shape parameters Circularity and Aspect Ratio*

cles caused by a cyclic loading. It grows with increasing number of cycles and correlates with the permanent volumetric strain. In contrast, negligible breakage was observed in other experimental work [41, 61, 63]. For a monotonic loading of sands partly or completely composed of crushable particles the amount of crushing has been found dependent on stress level, void ratio and particle characteristics (size, grading, shape, strength, mineral composition) [2, 10, 11, 24, 38, 39, 46, 49, 50].

6   Influence of sample dimensions

In the present study samples with a height-to-diameter ratio of $h/d = 1$ were tested, while samples with $h/d = 2$ are more common internationally. While both geometries are standard in the German code DIN 18137, the 1:1 samples are more frequently used in experimental studies dedicated to constitutive modeling since they are believed to deform more homogeneously. In the following the influence of the sample dimensions is discussed based on an additional test series performed on the natural sand. Beside the 1:1 and 2:1 samples with a diameter of 100 mm, also smaller ($d = 50$ mm) and larger ($d = 150$ mm) 1:1 samples have been tested. Schemes of the different sample dimensions are provided at the top of Figure 18.

The first row of diagrams in Figure 18 presents results

of drained monotonic triaxial tests. A loose and a dense sample were tested for each sample geometry. The principal shape of the curves $q(\varepsilon_1)$ and $\varepsilon_v(\varepsilon_1)$ (Figure 18a,b) is quite similar for the different sample dimensions, with the only exception that the curve $q(\varepsilon_1)$ measured for the dense 2:1 sample reaches its peak at a slightly lower axial strain. The deviations of the curves in Figure 18a,b are mainly due to the variations in initial relative density. The φ_P-I_{D0} diagram in Figure 18c reveals, however, an influence of the sample geometry on the peak friction angle. At low densities, the 2:1 samples with $d = 100$ mm show an about 2° lower peak friction angles than the 1:1 samples of same diameter. These differences decrease with increasing density. The φ_P data for the samples with $d = h = 150$ mm agree well with those for $d = h = 100$ mm, while the values for $d = h = 50$ mm are again about 1° to 1.5° higher. The differences in the peak friction angles between the 1:1 and 2:1 samples may be due to the different pattern of shear bands in the samples [13]. The higher φ_P values for the smallest sample geometry may be the result of a larger influence of end restraints. In contrast to [4], increasing the number of lubrication layers (e.g. using two layers of grease and rubber disk at each end plate) was found ineffective regarding a further reduction of φ_P for the 1:1 samples with $d = 100$ mm in another series of tests on a fine sand [83].

14

Since the present study concentrates on the cumulative behaviour under cyclic loading, the influence of the sample geometry in cyclic tests is of larger interest. The second row of diagrams in Figure 18 presents a comparison of cyclic tests performed with the four different sample dimensions. For each geometry several samples with different initial relative densities were tested. Neither the strain accumulation curves $\varepsilon^{\mathrm{acc}}(N)$ for medium dense samples in Figure 18d nor the relationship between the accumulated strain $\varepsilon^{\mathrm{acc}}$ after 10^5 cycles and the initial relative density I_{D0} in Figure 18e nor the plot of deviatoric strain $\varepsilon_q^{\mathrm{acc}}(N = 10^5)$ versus volumetric strain $\varepsilon_v^{\mathrm{acc}}(N = 10^5)$ in Figure 18f show a distinct influence of the sample dimensions. Therefore, it can be concluded that the results of the cyclic tests presented in this paper are not significantly affected by the (unusual) sample geometry.

7 Summary, conclusions and outlook

Three granular materials with significantly different grain shape and surface characteristics have been studied in drained cyclic triaxial tests. The glass beads, the natural sand with its subrounded grains and the crushed sand with its very angular particles were tested with the same specially mixed grain size distribution curve. Four test series with different amplitudes, densities, average mean pressures and average stress ratios were performed on each material. The maximum number of cycles (10^5) was the same in all tests.

The direction of accumulation, i.e. the ratio $\dot{\varepsilon}_v^{\mathrm{acc}}/\dot{\varepsilon}_q^{\mathrm{acc}}$ of the volumetric and deviatoric strain accumulation rates, was found almost independent of amplitude, density and average mean pressure for all three tested materials. It is mainly determined by the average stress ratio η^{av}. While $\dot{\varepsilon}_q^{\mathrm{acc}} = 0$ (purely isotropic strain accumulation) was approximately fulfilled for isotropic average stresses ($\eta^{\mathrm{av}} = 0$) independently of grain shape, the stress ratio $\eta^{\mathrm{av}} = M_{cc}$ corresponding to a purely deviatoric strain accumulation ($\dot{\varepsilon}_v^{\mathrm{acc}} = 0$) grows with increasing angularity of the particles, due to the higher interparticle friction and interlocking between adjacent grains.

The curves of accumulated strain $\varepsilon^{\mathrm{acc}}$ versus the number of cycles N are also affected by the grain shape. For the crushed sand they run almost proportional to $\ln(N)$ up to $N = 10^5$. For the natural sand and the glass beads $\varepsilon^{\mathrm{acc}}(N) \sim \ln(N)$ is obeyed only up to $N = 10^4$. At larger number of cycles the inclination of the curves in $\varepsilon^{\mathrm{acc}}$-$N$ diagrams with semi-logarithmic scale increases.

The higher interparticle friction and interlocking in the more angular materials affects also the intensity of strain accumulation. While for glass beads and natural sand the residual strain at $N = 10^5$ grows almost proportional to the square of the stress amplitude, an approximately linear relationship between $\varepsilon^{\mathrm{acc}}$ and q^{ampl} has been observed for the crushed sand. The largest differences between the various grain shapes are obvious in the pressure dependence of the strain accumulation rates. While the glass beads and (less pronounced) the natural sand showed a decrease of the residual strain with increasing values of average mean pressure p^{av}, it was the other way around for the crushed sand. Due to the larger potential for grain rearrangements by rolling and sliding, at low pressures ($p^{\mathrm{av}} = 50$ kPa) the accumulation of strain was higher in the glass beads than in the natural sand and in particular in the crushed sand.

The differences diminished at higher pressures ($p^{\mathrm{av}} = 300$ kPa), however. This is probably a result of the increase of the deformations at the grain contacts with growing pressure, which render the contact behaviour almost independent of the original shape. The relationships between residual strain and relative density or average stress ratio were found quite similar for the three tested grain shapes, with the dependencies being slightly less pronounced for the crushed sand. For all test conditions the strain amplitudes (elastic portion of deformation) measured for the crushed sand were larger than those observed for the other two materials, due to the higher void ratio at same relative density, the lower coordination number and the weaker response of the angular contacts.

Based on the experimental data the parameters of the high-cycle accumulation (HCA) model of Niemunis et al. [51] have been calibrated. The function f_p had to be extended by an additional term in order to adequately describe the data collected for the glass beads. The HCA model parameters have been analyzed in dependence on grain shape parameters determined from an automated analysis. The parameters C_{ampl}, C_p, C_Y and C_{N3} were found to increase with increasing circularity and decreasing aspect ratio of the particles, while the opposite tendency (C_{N1}) or no clear correlation (C_e, C_{N2}) were observed for the remaining parameters.

Currently, the experimental investigation is extended to several other natural sands with varying grain shape. Based on the available and complemented data the simplified calibration procedure for the HCA model parameters will be extended by the influence of the grain shape in future.

References

[1] M. M. Ahmadi and N. A. Paydar. Requirements for soil-specific correlation between shear wave velocity and liquefaction resistance of sands. *Soil Dynamics and Earthquake Engineering*, 57:152–163, 2014.

[2] F.N. Altuhafi and M.R. Coop. Changes to particle characteristics associated with the compression of sands. *Géotechnique*, 61(6):459–471, 2011.

[3] K.H. Andersen and K. Schjetne. Database of friction angles of sand and consolidation characteristics of sand, silt, and clay. *Journal of Geotechnical and Geoenvironmental Engineering, ASCE*, 139(7):1140–1155, 2013.

[4] A.W. Bishop and G.E. Green. The influence of end restraint on the compression strength of a cohesionless soil. *Géotechnique*, 15(3):243–266, 1965.

[5] G. Bouckovalas, R.V. Whitman, and W.A. Marr. Permanent displacement of sand with cyclic loading. *Journal of Geotechnical Engineering, ASCE*, 110(11):1606–1623, 1984.

[6] S. F. Brown. Repeated load testing of a granular material. *Journal of the Geotechnical Engineering Division, ASCE*, 100(7):825 – 841, 1974.
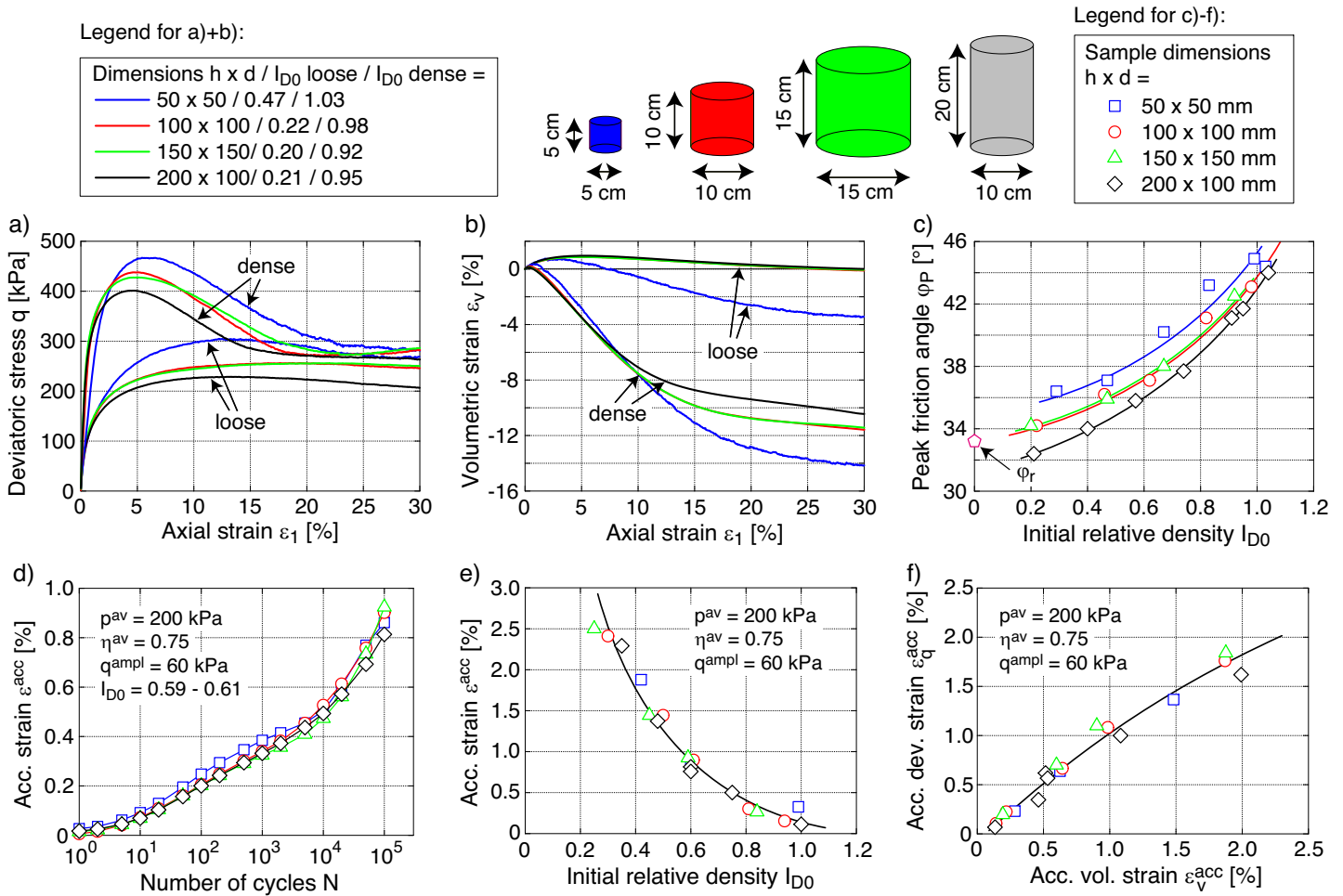
Fig. 18: *Influence of sample geometry on the results of drained monotonic triaxial tests on the natural sand: a) Stress-strain curves $q(\varepsilon_1)$, b) volumetric strain $\varepsilon_v(\varepsilon_1)$, c) density-dependent peak friction angle $\varphi_P(I_{D0})$; Influence of sample geometry on the results of drained cyclic triaxial tests on the natural sand: d) Strain accumulation curves $\varepsilon^{acc}(N)$ for medium density, e) accumulated strain ε^{acc} after $N = 10^5$ cycles as a function of initial relative density I_{D0}, f) accumulated deviatoric strain $\varepsilon_q^{acc}(N = 10^5)$ versus accumulated volumetric strain $\varepsilon_v^{acc}(N = 10^5)$ after 10^5 cycles*

[7] I. Cavarretta, M. Coop, and C. O'sullivan. The influence of particle characteristics on the behaviour of coarse grained soils. *Géotechnique*, 60(6):413–423, 2010.

[8] C.S. Chang and R.V. Whitman. Drained permanent deformation of sand due to cyclic loading. *Journal of Geotechnical Engineering, ASCE*, 114(10):1164–1180, 1988.

[9] G.-C. Cho, J. Dodds, and J.C. Santamarina. Particle shape effects on packing density, stiffness, and strength: natural and crushed sands. *Journal of Geotechnical and Geoenvironmental Engineering, ASCE*, 132(5):591–602, 2006.

[10] M.R. Coop. The mechanics of uncemented carbonate sands. *Géotechnique*, 40(4):607–626, 1990.

[11] M.R. Coop, K.K. Sorensen, T. Bodas Freitas, and G. Georgoutos. Particle breakage during shearing of a carbonate sand. *Géotechnique*, 54(3):157–163, 2004.

[12] M.R. Cox and M. Budhu. A practical approach to grain shape quantification. *Engineering Geology*, 96:1–16, 2008.

[13] J. Desrues, R. Chambon, M. Mokni, and F. Mazerolle. Void ratio evolution inside shear bands in triaxial sand specimens studied by computed tomography. *Géotechnique*, 46(3):529–546, 1996.

[14] V.A. Diyaljee and G.P. Raymond. Repetitive load deformation of cohesionless soil. *Journal of the Geotechnical Engineering Division, ASCE*, 108(GT10):1215–1229, 1982.

[15] S. Donohue, C. O'Sullivan, and M. Long. Particle breakage during cyclic triaxial loading of a carbonate sand. *Géotechnique*, 59(5):477–482, 2009.

[16] P.M. Duku, J.P. Stewart, D.H. Whang, and E. Yee. Volumetric strains of clean sands subject to cyclic loads. *Journal of Geotechnical and Geoenvironmental Engineering, ASCE*, 134(8):1073–1085, 2008.

[17] L. Flemming. Studies of the surface characteristics of sand particles (in German). Diploma thesis, Institute for Soil Mechanics and Rock Mechanics, Karlsruhe Institute of Technology (KIT), 2015.

[18] R. Galindo, M. Illueca, and R. Jimenez. Permanent deformation estimates of dynamic equipment foundations: Application to a gas turbine in granular soils. *Soil Dynamics and Earthquake Engineering*, 63(1):8–18, 2014.

[19] J.D. Goddard. Nonlinear elasticity and pressure-dependent wave speeds in granular media. *Proceedings of the Royal Society London*, 430:105–131, 1990.

[20] U. Gori and M. Mari. The correlation between the fractal dimension and internal friction angle of different granular materials. *Soils and Foundations*, 41(6):17–23, 2001.

[21] A. Gotschol. Veränderlich elastisches und plastisches Verhalten nichtbindiger Böden und Schotter unter zyklisch-dynamischer Beanspruchung. Dissertation, Universität Gh Kassel, 2002.

[22] P. Guo and X. Su. Shear strength, interparticle locking, and dilatancy of granular materials. *Canadian Geotechnical Journal*, 44(5):579–591, 2007.

[23] A. Ham, J. Wang, and J.G. Stammer. Relationships between particle shape characteristics and macroscopic damping in dry sands. *Journal of Geotechnical and Geoenvironmental Engineering, ASCE*, 138(8):1002–1011, 2012.

[24] B. Hardin. Crushing of soil particles. *Journal of Geotechnical Engineering, ASCE*, 111(10):1177–1192, 1985.

[25] H. Hertz. Über die Berührung fester elastischer Körper. *Journal reine und angewandte Mathematik*, 92:156–171, 1881.

[26] M. Hyodo, N. Aramaki, M. Itoh, and A.F.L. Hyde. Cyclic strength and deformation of crushable carbonate sand. *Soil Dynamics and Earthquake Engineering*, 15(5):331–336, 1996.

[27] M. Hyodo, A.F.L. Hyde, and N. Aramaki. Liquefaction of crushable soils. *Géotechnique*, 48(4):527–543, 1998.

[28] B. Indraratna, J. Lackenby, and D. Christie. Effect of confining pressure on the degradation of ballast under cyclic loading. *Géotechnique*, 55(4):325–328, 2005.

[29] S. Jänke. Zusammendrückbarkeit und Scherfestigkeit nichtbindiger Erdstoffe - ihre quantitative Ermittlung mit Hilfe einfacher Kennwerte und Feststellung der sie bestimmenden Einflußfaktoren. *Baumaschine und Bautechnik*, 15(3):91–101, 1968.

[30] W.S. Kaggwa, J.R. Booker, and J.P. Carter. Residual strains in calcareous sand due to irregular cyclic loading. *Journal of Geotechnical Engineering, ASCE*, 117(2):201–218, 1991.

[31] C. Karg and W. Haegeman. Elasto-plastic long-term behavior of granular soils: Experimental investigation. *Soil Dynamics and Earthquake Engineering*, 29:155–172, 2009.

[32] R.M. Koerner. Effect of particle characteristics on soil strength. *Journal of the Soil Mechanics and Foundations Division, ASCE*, 96(SM4):1221–1234, 1970.

[33] T. Kokusho, T. Hara, and R. Hiraoka. Undrained shear strength of granular soils with different particle gradations. *Journal of Geotechnical and Geoenvironmental Engineering, ASCE*, 130(6):621–629, 2004.

[34] S.L. Kramer. *Geotechnical earthquake engineering.* Prentice-Hall, Upper Saddle River, N.J., 1996.

[35] W. Krumbein. Measurement and geological significance of shape and roundness of sedimentary particles. *Journal of Sedimentary Petrology*, 11(2):64–72, 1941.

[36] W. C. Krumbein and L. L. Sloss. *Stratigraphy and sedimentation, 2nd Ed.* Freeman, San Francisco, 1963.

[37] J. Lackenby, B. Indraratna, G. McDowell, and D. Christie. Effect of confining pressure on ballast degradation and deformation under cyclic triaxial loading. *Géotechnique*, 57(6):527–536, 2007.

[38] P.V. Lade, J.A. Yamamuro, and P.A. Bopp. Significance of particle crushing in granular materials. *Journal of Geotechnical Engineering, ASCE*, 122(4):309–316, 1996.

[39] S.L. Leleu and J.R. Valdes. Experimental study of the influence of mineral composition on sand crushing. *Géotechnique*, 57(3):313–317, 2007.

[40] Q.B. Liu and B.M. Lehane. The influence of particle shape on the (centrifuge) cone penetration test (CPT) end resistance in uniformly graded granular soils. *Géotechnique*, 62(11):973–984, 2012.

[41] S. López-Querol and M.R. Coop. Drained cyclic behaviour of loose Dogs Bay sand. *Géotechnique*, 62(4):281–289, 2012.

[42] M.P. Luong. Mechanical aspects and thermal effects of cohesionless soils under cyclic and transient loading. In *Proc. IUTAM Conf. on Deformation and Failure of Granular materials, Delft*, pages 239–246, 1982.

[43] K. Mair, K.M. Frye, and C. Marone. Influence of grain characteristics on the friction of granular shear zones. *Journal of Geophysical Research*, 107(B10):ECV–4–1–ECV–4–9, 2002.

[44] W.A. Marr and J.T. Christian. Permanent displacements due to cyclic wave loading. *Journal of the Geotechnical Engineering Division, ASCE*, 107(GT8):1129–1149, 1981.

[45] H. Matsuoka and T. Nakai. A new failure criterion for soils in three-dimensional stresses. In *Deformation and Failure of Granular Materials*, pages 253–263, 1982. Proc. IUTAM Symp. in Delft.

[46] G.R. McDowell and M.D. Bolton. On the micromechanics of crushable aggregates. *Géotechnique*, 48(5):667–679, 1998.

[47] K. Miura, K. Maeda, M. Fureukawa, and S. Toki. Physical characteristics of sands with different primary properties. *Soils and Foundations*, 37(3):53–64, 1997.

[48] K. Miura, K. Maeda, M. Furukawa, and S. Toki. Mechanical characteristics of sands with different primary properties. *Soils and Foundations*, 38(4):159–172, 1998.

[49] Y. Nakata, A.F.L. Hyde, M. Hyodo, and H. Murata. A probabilistic approach to sand particle crushing in the triaxial test. *Géotechnique*, 49(5):567–583, 1999.

[50] Y. Nakata, M. Hyodo, A.F.L. Hyde, Y. Kato, and H. Murata. Microscopic particle crushing of sand subjected to high pressure one dimensional compression. *Soils and Foundations*, 41(1):69–82, 2001.

[51] A. Niemunis, T. Wichtmann, and Th. Triantafyllidis. A high-cycle accumulation model for sand. *Computers and Geotechnics*, 32(4):245–263, 2005.

[52] M. Oda. Anisotropic strength of cohesionless sands. *Journal of the Geotechnical Engineering Division, ASCE*, 107(9):1219–1231, 1981.

[53] V.A. Osinov. Application of a high-cycle accumulation model to the analysis of soil liquefaction around a vibrating pile toe. *Acta Geotechnica*, 8(6):675–684, 2013.

[54] W.H. Peacock and H.B. Seed. Sand liquefaction under cyclic loading simple shear conditions. *Journal of the Soil Mechanics and Foundations Division, ASCE*, 94(SM3):689–708, 1968.

[55] M.C. Powers. A new roundness scale for sedimentary particles. *Journal of Sedimentary Petrology*, 23(2):117–119, 1953.

[56] A. Quadimi and M.R. Coop. The undrained cyclic behaviour of a carbonate sand. *Géotechnique*, 57(9):739–750, 2007.

[57] G.P. Raymond and D.R. Williams. Repeated load triaxial tests on a dolomite ballast. *Journal of Geotechnical Engineering, ASCE*, 104:1013–1029, 1978.

[58] G. Rittenhouse. A visual method of estimating two-dimensional sphericity. *Journal of Sedimentary Petrology*, 13(2):79–81, 1943.

[59] P.C. Rousé, R.J. Fannin, and D.A. Shuttle. Influence of roundness on the void ratio and strength of uniform sand. *Géotechnique*, 58(3):227–231, 2008.

[60] A. Sadrekarimi and S.M. Olson. Critical state friction angle of sands. *Géotechnique*, 61(9):771–783, 2011.

[61] M. Salem, H. Elmamlouk, and S. Agaiby. Static and cyclic behavior of North Coast calcareous sand in Egypt. *Soil Dynamics and Earthquake Engineering*, 55(10):83–91, 2013.

[62] S.B.M. Salleh. *Cyclic loading of carbonate sand.* PhD thesis, University of Bradford, 1992.

[63] E.A. Sandoval and M.A. Pando. Experimental assessment of the liquefaction resistance of calcareous biogeneous sands. *Earth Science Research Journal*, 16(1), 2012.

[64] C. Santamarina. Soil phenomena at the particle/pore scale. Presentation at IBF, KIT, December, 2012.

[65] A. Sawicki and W. Świdziński. Compaction curve as one of basic characteristics of granular soils. In E. Flavigny and D. Cordary, editors, *4th Colloque Franco-Polonais de Mechanique des Sols Appliquee*, volume 1, pages 103–115, 1987. Grenoble.

[66] A. Sawicki and W. Świdziński. Mechanics of a sandy subsoil subjected to cyclic loadings. *International Journal For Numerical And Analytical Methods in Geomechanics*, 13(5):511–529, 1989.

[67] A. Sezer, S. Altun, and B.A. Göktepe. Relationships between shape characteristics and shear strength of sands. *Soils and Foundations*, 51(5):857–871, 2011.

[68] J.T. Shahu and Yudhbir. Model tests on sands with different angularity and mineralogy. *Soils and Foundations*, 38(4):151–158, 1998.

[69] M. J. Shenton. Deformation of railway ballast under repeated loading conditions. In *Railroad Track Mechanics and Technology*, pages 405 – 425. Pergamon Press, 1978.

[70] H. Shin and J.C. Santamarina. Role of particle angularity on the mechanical behavior of granular mixtures. *Journal of Geotechnical and Geoenvironmental Engineering, ASCE*, 139(2):353–355, 2013.

[71] M.L. Silver and H.B. Seed. Deformation characteristics of sands under cyclic loading. *Journal of the Soil Mechanics and Foundations Division, ASCE*, 97(SM8):1081–1098, 1971.

[72] M.L. Silver and H.B. Seed. Volume changes in sands during cyclic loading. *Journal of the Soil Mechanics and Foundations Division, ASCE*, 97(SM9):1171–1182, 1971.

[73] A.S.J. Suiker, E.T. Selig, and R. Frenkel. Static and cyclic triaxial testing of ballast and subballast. *Journal of Geotechnical and Geoenvironmental Engineering, ASCE*, 131(6):771–782, 2005.

[74] B. Sukumaran and A.K. Ashmawy. Quantitative characterisation of the geometry of discrete particles. *Géotechnique*, 51(7):619–627, 2001.

[75] F. Tatsuoka. Impacts on geotechnical engineering of several recent findings from laboratory stress-strain tests on geomaterials. In A.G. Correia and H. Brandl, editors, *Geotechnics for roads, rail tracks and earth structures*. Balkema, A.A., 2001.

[76] F. Tatsuoka, S. Maeda, K. Ochi, and S. Fujii. Prediction of cyclic undrained strength of sand subjected to irregular loadings. *Soils and Foundations*, 26(2):73–89, 1986.

[77] F. Tatsuoka, S. Toki, S. Miura, H. Kato, M. Okamoto, S.-I. Yamada, S. Yasuda, and F. Tanizawa. Some factors affecting cyclic undrained triaxial strength of sand. *Soils and Foundations*, 26(3):99–116, 1986.

[78] D.H. Timmerman and T.H. Wu. Behavior of dry sands under cyclic loading. *Journal of the Soil Mechanics and Foundations Division, ASCE*, 95(SM4):1097–1112, 1969.

[79] A. Tsomokos and V.N. Georgiannou. Effect of grain shape and angularity on the undrained response of fine sands. *Canadian Geotechnical Journal*, 47(5):539–551, 2010.

[80] Y.P. Vaid, J.C. Chern, and H. Tumi. Confining pressure, grain angularity and liquefaction. *Journal of Geotechnical Engineering, ASCE*, 111(10):1229–1235, 1985.

[81] L.M. Wei and J. Yang. On the role of grain shape in static liquefaction of sand-fines mixtures. *Géotechnique*, 64(9):740–745, 2014.

[82] T. Wichtmann. Explicit accumulation model for non-cohesive soils under cyclic loading. PhD thesis, Publications of the Institute of Soil Mechanics and Foundation Engineering, Ruhr-University Bochum, Issue No. 38, 2005.

[83] T. Wichtmann. Soil behaviour under cyclic loading - experimental observations, constitutive description and applications. Habilitation thesis, Publications of the Institute of Soil Mechanics and Rock Mechanics, Karlsruhe Institute of Technology, Issue No. 181, 2016.

[84] T. Wichtmann, A. Niemunis, and Th. Triantafyllidis. Strain accumulation in sand due to cyclic loading: drained triaxial tests. *Soil Dynamics and Earthquake Engineering*, 25(12):967–979, 2005.

[85] T. Wichtmann, A. Niemunis, and Th. Triantafyllidis. Experimental evidence of a unique flow rule of non-cohesive soils under high-cyclic loading. *Acta Geotechnica*, 1(1):59–73, 2006.

[86] T. Wichtmann, A. Niemunis, and Th. Triantafyllidis. On the influence of the polarization and the shape of the strain loop on strain accumulation in sand under high-cyclic loading. *Soil Dynamics and Earthquake Engineering*, 27(1):14–28, 2007.

[87] T. Wichtmann, A. Niemunis, and Th. Triantafyllidis. Strain accumulation in sand due to cyclic loading: drained cyclic tests with triaxial extension. *Soil Dynamics and Earthquake Engineering*, 27(1):42–48, 2007.

[88] T. Wichtmann, A. Niemunis, and Th. Triantafyllidis. Validation and calibration of a high-cycle accumulation model based on cyclic triaxial tests on eight sands. *Soils and Foundations*, 49(5):711–728, 2009.

[89] T. Wichtmann, A. Niemunis, and Th. Triantafyllidis. On the determination of a set of material constants for a high-cycle accumulation model for non-cohesive soils. *International Journal For Numerical And Analytical Methods in Geomechanics*, 34(4):409–440, 2010.

[90] T. Wichtmann, A. Niemunis, and Th. Triantafyllidis. On the ”elastic” stiffness in a high-cycle accumulation model for sand: a comparison of drained and undrained cyclic triaxial tests. *Canadian Geotechnical Journal*, 47(7):791–805, 2010.

[91] T. Wichtmann, A. Niemunis, and Th. Triantafyllidis. Towards the FE prediction of permanent deformations of offshore wind power plant foundations using a high-cycle accumulation model. In *International Symposium: Frontiers in Offshore Geotechnics, Perth, Australia*, pages 635–640, 2010.

[92] T. Wichtmann, A. Niemunis, and Th. Triantafyllidis. On the "elastic stiffness" in a high-cycle accumulation model - continued investigations. *Canadian Geotechnical Journal*, 50(12):1260–1272, 2013.

[93] T. Wichtmann, A. Niemunis, and Th. Triantafyllidis. Flow rule in a high-cycle accumulation model backed by cyclic test data of 22 sands. *Acta Geotechnica*, 9(4):695–709, 2014.

[94] T. Wichtmann, A. Niemunis, and Th. Triantafyllidis. Improved simplified calibration procedure for a high-cycle accumulation model. *Soil Dynamics and Earthquake Engineering*, 70(3):118–132, 2015.

[95] T. Wichtmann, H.A. Rondón, A. Niemunis, Th. Triantafyllidis, and A. Lizcano. Prediction of permanent deformations in pavements using a high-cycle accumulation model. *Journal of Geotechnical and Geoenvironmental Engineering, ASCE*, 136(5):728–740, 2010.

[96] T. Wichtmann and Th. Triantafyllidis. Über den Einfluss der Kornverteilungskurve auf das dynamische und das kumulative Verhalten nichtbindiger Böden. *Bautechnik*, 82(6):378–386, 2005.

[97] T. Wichtmann and Th. Triantafyllidis. Inspection of a high-cycle accumulation model for large numbers of cycles (N = 2 million). *Soil Dynamics and Earthquake Engineering*, 75:199–210, 2015.

[98] R.T. Wong, H.B. Seed, and C.K. Chan. Cyclic loading liquefaction of gravelly soils. *Journal of the Geotechnical Engineering Division, ASCE*, 101(GT6):571–583, 1975.

[99] Y.F. Xu and D.A. Sun. Correlation of surface fractal dimension with frictional angle at critical state of sands. *Géotechnique*, 55(9):691–695, 2005.

[100] S. Yasuda and M. Soga. Effects of frequency on undrained strength of sands (in Japanese). In *Proc. 19th Nat. Conf. Soil Mech. Found. Eng.*, pages 549–550, 1984.

[101] E. Yee, P. M. Duku, and J. P. Stewart. Cyclic volumetric strain behavior of sands with fines of low plasticity. *Journal of Geotechnical and Geoenvironmental Engineering, ASCE*, 140:1–10, 2014.

[102] Y. Yoshimi and H. Oh-Oka. Influence of degree of shear stress reversal on the liquefaction potential of saturated sand. *Soils and Foundations*, 15(3):27–40, 1975.

[103] T.L. Youd. Compaction of sands by repeated shear straining. *Journal of the Soil Mechanics and Foundations Division, ASCE*, 98(SM7):709–725, 1972.

[104] H. Zachert. Zur Gebrauchstauglichkeit von Gründungen für Offshore-Windenergieanlagen. Dissertation, Veröffentlichungen des Institutes für Bodenmechanik und Felsmechanik am Karlsruher Institut für Technologie, Heft Nr. 180, 2015.

[105] H. Zachert, T. Wichtmann, P. Kudella, T. Triantafyllidis, and U. Hartwig. Validation of a high cycle accumulation model via FE-simulations of a full-scale test on a gravity base foundation for offshore wind turbines. In *International Wind Engineering Conference, IWEC 2014, Hannover*, 2014.

[106] H. Zachert, T. Wichtmann, T. Triantafyllidis, and U. Hartwig. Simulation of a full-scale test on a Gravity Base Foundation for Offshore Wind Turbines using a High Cycle Accumulation Model. In *3rd International Symposium on Frontiers in Offshore Geotechnics (ISFOG), Oslo*, 2015.

[107] H. Zachert, T. Wichtmann, and Th. Triantafyllidis. Soil structure interaction of foundations for offshore wind turbines. In *26th International Ocean and Polar Engineering Conference (ISOPE-2016), Rhodos*, 2016.

[108] L. Zhuang, Y. Nakata, U.-G. Kim, and D. Kim. Influence of relative density, particle shape, and stress path on the plane strain compression behavior of granular materials. *Acta Geotechnica*, 9(2):241–255, 2014.

Appendix: Equations of the HCA model

The HCA model has been originally proposed by Niemunis et al. [51] in 2005. The model is based on the comprehensive experimental parametric study documented in [82, 84–87]. Deficits (lack of generality, missing influencing parameters, 1D formulation) of older HCA models proposed in the literature [5, 14, 21, 30, 44, 65, 66] have been discussed in [82].

The basic equation of the HCA model reads

$$\dot{\boldsymbol{\sigma}} = \mathsf{E} : (\dot{\boldsymbol{\varepsilon}} - \dot{\boldsymbol{\varepsilon}}^{\mathrm{acc}} - \dot{\boldsymbol{\varepsilon}}^{\mathrm{pl}}) \tag{3}$$

with the stress rate $\dot{\boldsymbol{\sigma}}$ of the effective Cauchy stress $\boldsymbol{\sigma}$ (compression positive), the strain rate $\dot{\boldsymbol{\varepsilon}}$ (compression positive), the accumulation rate $\dot{\boldsymbol{\varepsilon}}^{\mathrm{acc}}$, a plastic strain rate $\dot{\boldsymbol{\varepsilon}}^{\mathrm{pl}}$ (necessary only for stress paths touching the yield surface) and the barotropic elastic stiffness E. In the context of HCA models the dot over a symbol means a derivative with respect to the number of cycles N (instead of time t), i.e. $\dot{\sqcup} = \partial \sqcup /\partial N$. Depending on the boundary conditions, Eq. (3) predicts either a change of average stress ($\dot{\boldsymbol{\sigma}} \neq \mathbf{0}$) or an accumulation of residual strain ($\dot{\boldsymbol{\varepsilon}} \neq \mathbf{0}$) or both.

For $\dot{\boldsymbol{\varepsilon}}^{\mathrm{acc}}$ in Eq. (3) the following multiplicative approach is used:

$$\dot{\boldsymbol{\varepsilon}}^{\mathrm{acc}} = \dot{\varepsilon}^{\mathrm{acc}} \, \mathbf{m} \tag{4}$$

with the *direction* of strain accumulation (flow rule) $\mathbf{m} = \dot{\boldsymbol{\varepsilon}}^{\mathrm{acc}}/\|\dot{\boldsymbol{\varepsilon}}^{\mathrm{acc}}\| = (\dot{\boldsymbol{\varepsilon}}^{\mathrm{acc}})^{\rightarrow}$ (unit tensor) and the *intensity* of strain accumulation $\dot{\varepsilon}^{\mathrm{acc}} = \|\dot{\boldsymbol{\varepsilon}}^{\mathrm{acc}}\|$. Based on the own test results [82, 85, 93] and corroborated by the literature [8, 42] the flow rule of the modified Cam clay (MCC) model is adopted for $\mathbf{m}$:

$$\mathbf{m} = \left[\frac{1}{3} \left(p^{\mathrm{av}} - \frac{(q^{\mathrm{av}})^2}{M^2 p^{\mathrm{av}}} \right) \mathbf{1} + \frac{3}{M^2} (\boldsymbol{\sigma}^{\mathrm{av}})^* \right]^{\rightarrow} \tag{5}$$

where $\sqcup^{\rightarrow} = \sqcup /\|\sqcup\|$ denotes the normalization of a tensorial quantity. For the triaxial case the critical stress ratio $M = F\, M_{cc}$ is calculated from

$$F = \begin{cases} 1 + M_{ec}/3 & \text{for } \eta^{\mathrm{av}} \leq M_{ec} \\ 1 + \eta^{\mathrm{av}}/3 & \text{for } M_{ec} < \eta^{\mathrm{av}} < 0 \\ 1 & \text{for } \eta^{\mathrm{av}} \geq 0 \end{cases} \tag{6}$$

wherein

$$M_{cc} = \frac{6 \sin \varphi_{cc}}{3 - \sin \varphi_{cc}} \quad \text{and} \quad M_{ec} = -\frac{6 \sin \varphi_{cc}}{3 + \sin \varphi_{cc}} \tag{7}$$

with parameter φ_{cc}.

The intensity of strain accumulation $\dot{\varepsilon}^{\mathrm{acc}}$ in Eq. (4) is calculated as a product of six functions:

$$\dot{\varepsilon}^{\mathrm{acc}} = f_{\mathrm{ampl}} \, \dot{f}_N \, f_e \, f_p \, f_Y \, f_\pi \tag{8}$$

each considering a single influencing parameter (see Table 3), i.e. the strain amplitude $\varepsilon^{\mathrm{ampl}}$ (function f_{ampl}), the cyclic preloading g^A ($\dot{f}_N$), void ratio e (f_e), average mean pressure p^{av} (f_p), average stress ratio η^{av} or $\bar{Y}^{\mathrm{av}}$ (f_Y) and the effect of polarization changes ($f_\pi = 1$ for a constant polarization as in the case of the test series presented in this paper).

Function	Material constants
$f_{\mathrm{ampl}} = \min \left\{ \left(\dfrac{\varepsilon^{\mathrm{ampl}}}{10^{-4}} \right)^{C_{\mathrm{ampl}}} ; 10^{C_{\mathrm{ampl}}} \right\}$	C_{ampl}
$\dot{f}_N = \dot{f}_N^A + \dot{f}_N^B$	C_{N1}
$\dot{f}_N^A = C_{N1} C_{N2} \exp \left[-\dfrac{g^A}{C_{N1} f_{\mathrm{ampl}}} \right]$	C_{N2}
$\dot{f}_N^B = C_{N1} C_{N3}$	C_{N3}
$f_e = \dfrac{(C_e - e)^2}{1 + e} \dfrac{1 + e_{\max}}{(C_e - e_{\max})^2}$	C_e
$f_p = \exp \left[-C_p \left(\dfrac{p^{\mathrm{av}}}{100 \text{ kPa}} - 1 \right) \right]$	C_p
$f_Y = \exp \left(C_Y \bar{Y}^{\mathrm{av}} \right)$	C_Y
$f_\pi = 1$ for constant polarization, [86]	

Table 3: Summary of the functions and material constants of the HCA model

The normalized stress ratio $\bar{Y}^{\mathrm{av}}$ used in f_Y is zero for isotropic stresses ($\eta^{\mathrm{av}} = 0$) and one on the critical state line ($\eta^{\mathrm{av}} = M_{cc}$). The function Y of Matsuoka & Nakai [45] is used for that purpose:

$$\bar{Y}^{\mathrm{av}} = \frac{Y^{\mathrm{av}} - 9}{Y_c - 9} \quad \text{with} \quad Y_c = \frac{9 - \sin^2 \varphi_{cc}}{1 - \sin^2 \varphi_{cc}} \tag{9}$$

$$Y^{\mathrm{av}} = \frac{27(3 + \eta^{\mathrm{av}})}{(3 + 2\eta^{\mathrm{av}})(3 - \eta^{\mathrm{av}})} \tag{10}$$

For a constant strain amplitude, the function f_N simplifies to:

$$f_N = C_{N1} \left[\ln(1 + C_{N2} N) + C_{N3} N \right] \tag{11}$$

The formulations of the functions f_{ampl}, f_N, f_e, f_p, f_Y, f_π have been chosen based on the own experimental results and documented data in the literature [6,14,57,65,66,71,72, 78,103]. They are also corroborated by more recent studies [16,28,37,73,101]. Since several experimental investigations in the literature reveal that the frequency does not influence the cumulative rates in sand under drained or undrained cyclic loading [16,31,33,54,56,69,76,77,98,100,102,103], the loading frequency is not considered as a parameter of the HCA model. While the parameter C_{ampl} of the amplitude function f_{ampl} was fixed to a value of 2.0 in earlier versions of the HCA model [51,82,89], later experimental results for various sands exhibited the need to introduce it as a material constant [94]. The extension of f_p as proposed by Eq. (2) represents another modification of the original HCA model formulation. Detailed investigations on the elastic stiffness E in Eq. (3) may be found in [90,92]. A more general formulation for the flow rule **m** enabling to consider anisotropy has been published in [95]. The large experimental effort for the calibration of the material constants of the HCA model lead to the development of a simplified calibration procedure based on correlations with the grain size distribution curve and index test results [88,94].